Discrepancies in temporal $p\mathrm{CO_2}$ variability from Earth System Models and $p\mathrm{CO_2}$-products related to high-latitude mixed layer dynamics and equatorial upwelling

Christopher Danek[1*] and Judith Hauck[1]

[1*]Alfred Wegener Institute for Polar and Marine Research (AWI), Am Handelshafen 12, Bremerhaven, 27570, Bremen, Germany.

*Corresponding author(s). E-mail(s): cdanek@awi.de;

Abstract

The air-sea $\mathrm{CO_2}$ flux $\boldsymbol{F}\mathrm{CO_2}$ is an important component of the global carbon budget and understanding its response to climate change is crucial to adjust mitigation pathways. Multi-linear regression supports the expectation that the balance between the $\mathrm{CO_2}$ partial pressures of air and the sea surface ($\boldsymbol{p}\mathrm{CO_2}$) is the most important driver of temporal $\boldsymbol{F}\mathrm{CO_2}$ variability. Discrepancies between state-of-the-art Earth System Models (ESMs) and gridded $\boldsymbol{p}\mathrm{CO_2}$-products suggest that systematic biases exist across an ensemble of ESMs. In the equatorial regions, upwelling variability of carbon-rich water is biased in ESMs as modeled and observed sea surface temperature are generally uncorrelated. In the high latitudes, the climate change induced trend towards lighter sea water is overestimated in ESMs, which yields - in contrast to observations - shallower mixed layers over the contemporary period and hence a suppressed carbon supply from depth. While mixed layer depth variability and trends appear biased throughout the global ocean, this is not a determining factor for $\boldsymbol{p}\mathrm{CO_2}$ variability in subtropical gyres. The results highlight the importance of accurately modeling hydrographic properties to obtain robust estimates of $\boldsymbol{F}\mathrm{CO_2}$ and its variability.

Keywords: Ocean $\mathrm{CO_2}$ uptake, air-sea $\mathrm{CO_2}$ flux, ocean ventilation and mixing, ocean dynamics

1 Introduction

Carbon dioxide (CO_2) emitted by human activities accumulates in the atmosphere and leads to global warming (Canadell et al, 2021). The world oceans act against this human-made climate change by taking up 26% of the total anthropogenic emissions since 1850 (additional 31% by the terrestrial biosphere; Friedlingstein et al, 2022). This flux of CO_2 between air and the sea surface (FCO_2) arises through and is proportional to the difference of the CO_2 partial pressures in air ($pCO_{2,\mathrm{atm}}$) and sea water (pCO_2), that tend to equilibrate, so that $FCO_2 \propto \Delta pCO_2 = pCO_2 - pCO_{2,\mathrm{atm}}$. The magnitude of FCO_2 further depends on the turbulence at the air-sea interface and the CO_2 solubility in sea water. Usually these effects are approximated as gas transfer velocity k_w via the wind stress exerted at the open ocean (i.e. not covered by sea ice $\mathrm{f}_{\mathrm{ice}}$; Wanninkhof, 1992, 2014; Garbe et al, 2014), and the decreasing CO_2 solubility $\phi^0_{CO_2}$ with increasing temperature (and salinity; Orr et al, 2017), yielding the usually utilized bulk formula $FCO_2 = k_w\,(1 - f_{\mathrm{ice}})\,\phi^0_{CO_2}\,\Delta pCO_2$. Defined like this, $FCO_2 < 0$ represents a flux of CO_2 from air into the sea (in moles or mass of carbon or CO_2 per unit area and time).

From a global perspective, observations (e.g., Sabine et al, 2004; Gruber et al, 2019) and models (e.g., Hauck et al, 2020; DeVries et al, 2023) indicate that ΔpCO_2 not only sets the sign but also dominates the magnitude of FCO_2 as the globally integrated ocean carbon sink (i.e. $FCO_2 < 0$) increased concurrently with the rising atmospheric CO_2 concentration ($CO_{2,\mathrm{atm}}$) and thereby more than doubled from -1.1 ± 0.4 PgC yr^{-1} in the 1960s to -2.8 ± 0.4 PgC yr^{-1} during 2011 to 2020 (PgC $= 10^{15}$ g of carbon; Friedlingstein et al, 2022), termed carbon-concentration feedback (Arora et al, 2020). Superimposed on this temporal $CO_{2,\mathrm{atm}}$-driven FCO_2 trend is a pronounced temporal variability on different time scales on the order of 20% of the trend (Gruber et al, 2023). As for the trend, $CO_{2,\mathrm{atm}}$ seems to act as the main driver of this temporal FCO_2 variability (McKinley et al, 2020), although the role of other factors such as internal variability of the climate system (e.g., McKinley et al, 2004; Landschützer et al, 2019), the meridional overturning circulation (e.g., Terhaar et al, 2022; Liu et al, 2022), surface winds (e.g., Lovenduski et al, 2007; Keppler and Landschützer, 2019), or the ocean's buffering capacity (e.g., Jiang et al, 2019) is an ongoing research question (Gruber et al, 2023; DeVries et al, 2023).

Understanding these carbon-climate feedbacks (Arora et al, 2020) is necessary to reliably estimate forthcoming $F\mathrm{CO}_2$ changes in our warming world. The ocean circulation in particular was shown to substantially affect $p\mathrm{CO}_2$ patterns (also termed circulation-driven $p\mathrm{CO}_2$ changes; e.g., Gallego et al, 2018; Gruber et al, 2019; DeVries, 2022). For example, Southern Ocean observations and model results suggest that an intensified ocean mixing increases the upper ocean carbon content, thereby affecting $F\mathrm{CO}_2$ (Wu et al, 2019; Kwak et al, 2021; Nicholson et al, 2022; Prend et al, 2022; Chen et al, 2022). Likewise, simulation results from Earth System Models (ESMs) indicate that a too strong stratification suppresses carbon and nutrient fluxes or uptake (Fu et al, 2016; Bourgeois et al, 2022; Fu et al, 2022). The exact mechanism, however, remains unclear since in ESMs a high stratification generally co-occurs with shallow mixed layers (Sallée et al, 2013), while in global observations mixed layer deepening trends were shown despite an increasing stratification over the historical period (Sallée et al, 2021).

Hence, given the substantial role of $\Delta p\mathrm{CO}_2 = p\mathrm{CO}_2 - p\mathrm{CO}_{2,\mathrm{atm}}$ in setting $F\mathrm{CO}_2$ and the relatively well known $\mathrm{CO}_{2,\mathrm{atm}}$ (as well as $p\mathrm{CO}_{2,\mathrm{atm}}$; Lan et al, 2023), we here investigate the ability of state-of-the-art ESMs of phase 6 of the Coupled Model Intercomparison Project (CMIP6; Eyring et al, 2016) to represent historical seawater $p\mathrm{CO}_2$ variability patterns. By identifying potential model biases we provide a foundation for a meaningful interpretation of the temporal variability of historical and scenario $F\mathrm{CO}_2$ estimates from ESMs, our most important tool for future climate projections and thus the basis of policy information and societal decision making (e.g., Canadell et al, 2021; Melnikova et al, 2021; Terhaar et al, 2022). Acknowledging uncertainties and overestimated variability in observation-based $p\mathrm{CO}_2$ estimates due to the limited number of observations (Gloege et al, 2021; Hauck et al, 2023), we compare multi-model CMIP6 simulation results to $p\mathrm{CO}_2$-products, gridded compilations of spatio-temporal sea surface $p\mathrm{CO}_2$ measurements (Bakker et al, 2016; Gregor and Fay, 2021). First, the drivers of the temporal global $F\mathrm{CO}_2$ variability are identified via multi-linear regression (e.g., Rödenbeck et al, 2022), reassuring the importance of $\Delta p\mathrm{CO}_2$ for temporal $F\mathrm{CO}_2$ variability. Second, temporal $p\mathrm{CO}_2$ variability discrepancies between CMIP6 models and $p\mathrm{CO}_2$-products are discussed. Finally, the identified model deficiencies, in particular the so far undocumented systematic bias in modeled temporal mixed layer depth trends, and $p\mathrm{CO}_2$ changes are set into perspective.

2 Methods

2.1 Temporal variability

To analyze the temporal variability of the ocean carbon sink we utilized various data sets of environmental variables which are described in this section. Time series of those are often dominated by a large temporal trend imposed by climate change. Following DeVries (2022), we here defined the interannual variability of a time series by subtracting its linear temporal trend. Positive values hence indicate time points at which a variable is greater than its linear trend and vice versa. Defined as such, the obtained anomalies with respect to the linear temporal trend of an annually averaged time series represent a range of temporal scales from year-to-year to sub-decadal to decadal, depending on the length of the annually averaged input time series. Additional averaging operators would allow for a more detailed distinction of temporal scales (e.g., Gloege et al, 2021; Mayot et al, 2023). Here, however, detrending was sufficient to identify temporal variability discrepancies between Earth System Models (ESMs) and observational data sets. Hereafter, interannual variability denotes temporal variability on year-to-year to decadal temporal scales with respect to the linear temporal trend.

2.2 Multi-linear regression of observed air-sea CO_2 flux

Driving factors of temporal air-sea CO_2 flux (FCO_2) variability were identified by multi-linear regression (Burnham and Anderson, 1998; Zuur et al, 2007). The predictant FCO_2 and the predictors atmospheric and sea surface CO_2 partial pressures $pCO_{2,\mathrm{atm}}$ and pCO_2 were taken from the SeaFlux data set (Fay et al, 2021; Gregor and Fay, 2021, version 2021.04.03). SeaFlux provides a gridded data ensemble based on global surface ocean CO_2 fugacity observations from SOCAT (Bakker et al, 2016), converted to FCO_2 and pCO_2 with external variables such as the atmospheric CO_2 concentration, sea level pressure, sea surface temperature, wind speed and sea ice and an air-sea gas exchange parameterization. Gap-filling algorithms such as multiple linear regression and neural networks were applied to the sparse observations to obtain the gridded product. Since different external data sets and extrapolation methods were used by different data sets creators, several realizations of FCO_2 and pCO_2 are included in SeaFlux, which together form an ensemble. Following Fay et al (2021), FCO_2 estimates based on the wind products CCMP2 (Atlas et al, 2011), ERA5 (Copernicus Climate Change Service, 2019) and JRA55 (Kobayashi et al, 2015) were considered in this study. Hence, the analyzed SeaFlux ensemble consists of six different pCO_2 and 18 different FCO_2 realizations (six times three different wind products).

Tab. 1 summarizes the 21 environmental variables which were utilized as predictors for interannual FCO_2 variability due to their known effects on the ocean carbon sink, as outlined in the introduction (e.g., DeVries, 2022; Rödenbeck et al, 2022; Gruber et al, 2023). All data sets were globally averaged/integrated before calculating the regression. Note that we conducted multi-linear regression not to find the best model to forecast FCO_2 (e.g., Lovenduski et al, 2019; Li et al, 2019), but to identify the origin of discrepancies of interannual FCO_2 variability between $p\mathrm{CO}_2$-products and ESMs (see section 2.3). The listed data sets were used as provided by the data sets creators, except the mixed layer depth (MLD) variables (see section 2.4).

Table 1: Data sets used as predictors for multi-linear regression of the SeaFlux ensemble mean FCO_2 from 1990 to 2019 (30 years; Gregor and Fay, 2021). All time series were annually averaged, spatially averaged/integrated over the same area, and detrended (temporal linear trend removed). ∂ denotes temporal difference, i.e. $\partial X(t) = X(t) - X(t-1)$ for year t.

No.	Predictor	Description and reference
1,2	$\mathrm{CO}_{2,\mathrm{atm}}$, $\partial\mathrm{CO}_{2,\mathrm{atm}}$	Atmospheric CO_2 concentration (Meinshausen et al, 2017)
3-5	$p\mathrm{CO}_{2,\mathrm{atm}}$, $\partial p\mathrm{CO}_{2,\mathrm{atm}}$, $p\mathrm{CO}_2$	Atmospheric and sea surface CO_2 partial pressure (Gregor and Fay, 2021)
6	$\Delta p\mathrm{CO}_2$	$p\mathrm{CO}_2 - p\mathrm{CO}_{2,\mathrm{atm}}$
7-10	W, W^2, W^3, W^4	Near-surface wind velocity from ERA5 (Copernicus Climate Change Service, 2019)
11,12	SST, ∂SST	Sea surface temperature SST from ERA5 (Copernicus Climate Change Service, 2019) or EN4.2.2 (Good et al, 2013)[a]
13,14	SSS, ∂SSS	Sea surface salinity SSS from EN4.2.2 (Good et al, 2013)
15,16	SIE_N, SIE_S	Northern and southern hemisphere sea ice extent (Fetterer et al, 2017)
17-20	$\mathrm{MLD}_{0.01}$, $\mathrm{MLD}_{0.03}$, $\mathrm{MLD}_{0.125}$, $\mathrm{MLD}_{\mathrm{HT09}}$	Mixed layer depth (MLD) via potential density ρ^θ criteria 0.01, 0.03 and 0.125 kg m^{-3} and from density algorithm of Holte and Talley (2009), all based on EN4.2.2 (Good et al, 2013)[b]
21	N34	Niño 3.4 anomaly index (Rayner, 2003)[b]

[a] Choice of SST data set did not substantially effect the regression results (not shown).
[b] See section 2.4.

The best multi-linear regression model was selected based on the minimum ΔIC (information criterion) for two IC, the corrected Akaike ($\mathrm{AIC_c}$) and the Bayesian information criteria (BIC). By definition, ΔIC equals 0 for the best model and two models are considered statistically different if their ΔIC differs by ≥ 2. If two models were identical based on this constraint, the model with the lower number of predictors n_pred was chosen (Burnham and Anderson, 1998; Zuur et al, 2007; Dziak et al, 2019). In addition, potential overfitting was avoided by excluding combinations of significantly correlated ($\mathrm{r} > 0.5$ with $\mathrm{p} < 0.05$) predictors (Bartoń, 2022).

2.3 Earth System Models (ESMs)

CMIP6 (Coupled Model Intercomparison Project Phase 6; Eyring et al, 2016) model output was obtained from the Earth System Grid Federation (Cinquini et al, 2014). The CMIP experiment historical (up to 2014) was extended with the ScenarioMIP experiment SSP1-2.6 (from 2015 onward), since its prescribed $CO_{2,atm}$ agrees best with measured $CO_{2,atm}$ (together with SSP1-1.9, not shown; O'Neill et al, 2016; Meinshausen et al, 2017; Lan et al, 2023). Most recent (vYYYYMMDD) files of one realization of each model and experiment was used (by default r1i1p1f1). Model output was processed on native grids (gn) if possible (see section 2.4). Availability of modeled atmosphere, ocean and ocean biogeochemistry variables chl (sea water chlorophyll from all modeled phytoplankton group concentrations), dpco2 (difference in partial pressure of carbon dioxide between sea water and air, i.e. ΔpCO_2), fgco2 (sea surface downward mass flux of carbon as CO_2, i.e. FCO_2), mlotst (ocean mixed layer thickness defined by a σ_θ threshold of 0.03 kg m^{-3}, i.e. $MLD_{0.03}$, see section 2.4), sfcWind (near-surface wind speed), so (sea water salinity), spco2 (surface aqueous partial pressure of CO_2, i.e. pCO_2), thetao (sea water potential temperature θ) and tos (sea surface temperature; https://github.com/PCMDI/cmip6-cmor-tables) lead to the selection of 10 ESMs listed in Tab. 2.

In addition to available CMIP6 model output we here include AWI-ESM-1-REcoM, a variant of AWI-CM-1 (Semmler et al, 2020) and AWI-ESM-1 (Danek et al, 2020) with the same model components for atmosphere (ECHAM6.3.04p1, Stevens et al, 2013; Giorgetta et al, 2013), terrestrial hydrological discharge (HDMODEL, Hagemann and Dümenil, 1998), terrestrial biogeochemistry (JSBACH3.20, Reick et al, 2021), and ocean and sea ice (FESOM1.4, Wang et al, 2014). Atmosphere and ocean were coupled hourly by OASIS3MCT_2.8 (Valcke et al, 2015; Craig et al, 2017). Details of individual model components can be found in the given references. In addition,

Table 2: CMIP6 ESMs analyzed in this study and their ocean model component. $\overline{d}_{\max}$ is the globally averaged horizontal ocean model resolution in km defined as $\sqrt{2\,A_e}$ with the surface area A_e of an irregular grid element for unstructured models (Danilov, 2022) or the maximum distance between horizontal grid cell vertices, i.e. $\sqrt{\Delta x^2 + \Delta y^2}$, for all other models (Taylor et al, 2018). n_{lev} is the number of vertical levels. The 'horizonal' and 'vertical' columns show tracer parameterizations utilized in the ocean model as identified in the given references (not meant to be complete; unstable stratification is compensated by some sort of fast and complete convection in all ocean models (Rahmstorf, 1993) and is omitted in the 'vertical' column). C87: Cox (1987), EPBL (energetic planetary boundary layer scheme): Reichl and Hallberg (2018), FFH: Fox-Kemper et al (2008), G95: Gent et al (1995), GM90: Gent and Mcwilliams (1990), KPP (k-profile parameterization): Large et al (1994), NK99: Noh and Jin Kim (1999), PP: Pacanowski and Philander (1981), R82: Redi (1982), TKE (turbulent kinetic energy scheme): Gaspar et al (1990).

No	ESM	Ocean model	$\overline{d}_{\max}$	n_{lev}	horizontal	vertical
1	AWI-ESM-1-REcoM (Semmler et al, 2020, this study)	FESOM1.4 (Wang et al, 2014)	76	46	R82, G95	KPP
2,3	CanESM5{-CanOE} (Swart et al, 2019)	NEMO3.4.1 (Saenko et al, 2018)	116	{41,45}	R82, GM90	TKE
4	CESM2-WACCM (Danabasoglu et al, 2020)	POP2 (Danabasoglu et al, 2012)	113	60	R82, GM90	KPP, FFH
5	CNRM-ESM2-1 (Séférian et al, 2019)	NEMO3.6 (Danabasoglu et al, 2014; Voldoire et al, 2019)	118	75	R82, GM90	TKE, FFH
6	GFDL-ESM4 (Dunne et al, 2020)	GFDL-OM4 (Adcroft et al, 2019)	59	75	R82, G95	EPBL, FFH
7	IPSL-CM6A-LR (Boucher et al, 2020)	NEMO3.6 (Boucher et al, 2020)	117	75	R82, GM90	TKE, FFH
8	MIROC-ES2L (Hajima et al, 2020)	COCO4.9 (Hasumi, 2015)	125	63	C87, GM90	NK99
9,10	MPI-ESM1-2-{HR,LR} (Mauritsen et al, 2019)	MPIOM1.63 (Marsland et al, 2003; Jungclaus et al, 2013)	{60,180}	40	R82, G95	PP, wind-driven turbulent mixing in mixed layer
11	UKESM1-0-LL (Sellar et al, 2019)	UK-GO6 (Storkey et al, 2018; Kuhlbrodt et al, 2018) based on NEMO3.6	117	75	R82, GM90	TKE

AWI-ESM-1-REcoM simulates the ocean biogeochemistry with the Regulated Ecosystem Model version 2 (REcoM2; Hauck et al, 2013; Schourup-Kristensen et al, 2014). REcoM2 routines are called in every ocean time step by the ocean and sea ice model FESOM1.4, i.e. the same spatial and temporal discretization applies to REcoM2. In FESOM1.4 (Finite Element Ocean Sea Ice Model) the governing equations are solved on an unstructured grid of tetrahedra of variable size with finite element methods (Danilov et al, 2004; Wang et al, 2008). Due to the variable horizontal resolution, dynamically important regions exhibit a relatively high spatial resolution down to ∼15 km (coastline, equator and high latitudes), while the quiescent interior of the world ocean gyres are resolved with a coarser resolution up to ∼120 km. This yields a global average of ∼76 km horizontal resolution (126 859 wet nodes) on 47 vertical levels ('core' mesh). Horizontal and vertical tracer parameterizations include mixing along isopycnals (Redi, 1982) and advection due to adiabatic stirring (Gent and Mcwilliams, 1990) implemented following Griffies et al (1998) with a background horizontal diffusion $K_{\mathrm{h},0}$ = 800 $m^2\ s^{-1}$. This value is lower compared to the 1 500 $m^2\ s^{-1}$ that was used in AWI-CM-1 (Semmler et al, 2020) and AWI-ESM-1 (Danek et al, 2020) experiments and was chosen due to improved model validation results (not shown). Further ocean and sea ice model details can be found in Wang et al (2014) and Timmermann et al (2009). REcoM2 simulates the carbonate system as well as element cycles of nitrate, silicic acid and iron. Two phytoplankton groups (small phytoplankton and diatoms) and a fast-growing small zooplankton group are represented. The phytoplankton stoichiometry depends on environmental conditions. Particle sinking arises due to aggregation of primary producers, sloppy feeding and defecation, and zooplankton mortality. Further details of the ocean biogeochemistry model REcoM2 used in this study can be found in Hauck et al (2013); Schourup-Kristensen et al (2014). Note that recent model development led to REcoM3 (Karakuş et al, 2021; Gürses et al, 2023), which differs from the setup utilized here. The AWI-ESM-1-REcoM simulations were conducted on concentration-driven mode and the experimental setup follows the CMIP6 protocols (Eyring et al, 2016). The piControl-spinup experiment was conducted for 736 years and ocean temperature and salinity were initialized from the PHC3.0 winter climatology (Steele et al, 2001). At the end of this spinup, the globally integrated air-sea CO_2 flux FCO_2 has a drift of 0.03 Pg C yr^{-1} century^{-1} towards zero, i.e. well below the 0.1 Pg C yr^{-1} century^{-1} threshold suggested by the C4MIP protocol (Coupled Climate–Carbon Cycle Model Intercomparison Project; Jones et al, 2016). A systematic analysis of the spinup of ocean and atmosphere physics as well as the ocean and land carbon cycle will be provided in a separate model description paper. The AWI-ESM-1-REcoM model data presented here will be added to the Earth System Grid Federation (Cinquini et al, 2014).

In the analyzed CMIP6 experiments (historical and scenario) the ocean carbon cycle is driven by the modeled physics of the coupled climate system, forced by prescribed atmospheric greenhouse gas concentrations (concentration-driven experiments; O'Neill et al, 2016; Meinshausen et al, 2017). In the CNRM-ESM2-1 model, in addition, variable carbon input from river runoff is prescribed. As a consequence, absolute values of FCO_2 differ substantially compared to other models (not shown; Séférian et al, 2019; Lacroix et al, 2020). Since we focus on centered (i.e. temporal mean removed) or detrended (i.e. linear temporal trend removed) time series, this poses no problem.

2.4 Post processing

Potential density ρ^θ (reference pressure $p_r = 0$ dbar) was calculated according to TEOS-10 (IOC et al, 2010; Kelley et al, 2022) from hydrographic EN4.2.2 data (Good et al, 2013) and ESM output. Based on ρ^θ the mixed layer depth (MLD) was calculated via different density thresholds 0.01, 0.03 and 0.125 kg m^{-3} ($MLD_{0.01}$, $MLD_{0.03}$, $MLD_{0.125}$; depth closest to 10 dbar was used as reference level) as well as Holte and Talley's density algorithm (MLD_{HT09}; Holte and Talley, 2009, http:

//mixedlayer.ucsd.edu/data/jaot09_holte_mld_algorithm_files.zip). For ESMs, the variable mlotst was used as $MLD_{0.03}$ if available. For comparison, temporal $MLD_{0.03}$ trends from Sallée et al (2021) were used, a data set based on the Word Ocean Database 2018, additional hydrographic profiles from PANGAEA, Argo floats and marine mammals equipped with hydrographic sensors (see references of these data sets in Sallée et al, 2021).

Area-weighted spatial averages/integrals were calculated globally and over biomes, which are defined based on environmental parameters that affect ocean carbon dynamics (SST, $MLD_{0.125}$, sea ice and chlorophyll Chl; Fay and McKinley, 2014). Following Gregor et al (2019), five super-biomes were investigated: northern and southern hemisphere high latitudes (NH-HL, SH-HL), sub-tropics (NH-ST, SH-ST) and the equatorial regions (EQU; https://github.com/RECCAP2-ocean/RECCAP2-shared-resources.git, version v20220620). In EQU, following Le Grix et al (2021), El Niño and La Niña events were identified if the monthly Niño 3.4 anomaly index (SST spatially averaged from 5°S to 5°N and 120°W to 170°W with the temporal mean from 1981-2010 removed; Rayner, 2003) exceeds ±0.4 for at least 6 months. In addition, the period of maximum temporal variability of equatorial SST was inferred from its frequency spectrum and tested for significance against red noise (Schulz and Mudelsee, 2002; Bunn et al, 2022) and normalized by its maximum (e.g., Landschützer et al, 2019).

Post processing steps were performed on the native grids of the data sets and ESMs if possible. If needed, conservative spatial remapping was used if possible, bilinear otherwise (i.e. operators 'remapycon' or 'remapbil' of Schulzweida, 2022). All reported correlations are significant ($p < 0.1$) if not stated otherwise. Linear trends were considered significant if the absolute trend exceeds its standard error. This is a more relaxed significance threshold than the usual $p < 0.1$, however, enables comparison with external data sets ($MLD_{0.03}$ trends from Sallée et al, 2021) and does not change the general interpretation of the shown results.

3 Results

3.1 Temporal FCO_2 variability

The global ocean is a CO_2 sink throughout the observational period from 1990 to 2019 (negative annual averages in Fig. 1a). The SeaFlux (Gregor and Fay, 2021) ensemble mean (thick gray-blue line) shows a slightly weakening ocean CO_2 uptake until 2001, followed by an intensification phase of FCO_2, i.e. a strengthened oceanic CO_2 uptake, also visible by the negative linear temporal trend (blue dashed line). The temporal mean and standard deviation of the pCO_2-product ensemble FCO_2 are -2.2 and 0.47 PgC yr^{-1}. Differences between FCO_2 realizations originate from the use of different pCO_2-products, as lines of different wind but identical pCO_2 are generally clustered. The annual and global averages of the corresponding surface ocean pCO_2-product is shown in Fig. 1b. pCO_2 is dominated by increasing anthropogenic $CO_{2,atm}$ over the observational period (red dashed line in Fig. 1b from Lan et al, 2023) and significantly correlated with FCO_2 (averaged over 3 wind products; numbers in labels in Fig. 1b; e.g. -0.9 for the ensemble mean, i.e. the globally averaged absolute pCO_2 explains 81% of the temporal variability of globally integrated absolute FCO_2). The corresponding $\Delta pCO_2 = pCO_2 - pCO_{2,atm}$ almost perfectly matches FCO_2 with correlations ≥ 0.97 in all pCO_2-products (Fig. 1c). The negative linear temporal trend of ΔpCO_2 (blue dashed line in (Fig. 1c) reflects the slower increase of pCO_2 compared to $CO_{2,atm}$. Note that in the late 1990s some pCO_2-products exhibit global $\Delta pCO_2 > 0$ despite global $FCO_2 < 0$. This sign discrepancy may arise if a region exhibits locations of positive and negative ΔpCO_2 and if unequal weights are applied to these locations in the bulk formula by e.g. low and high wind speeds, respectively.

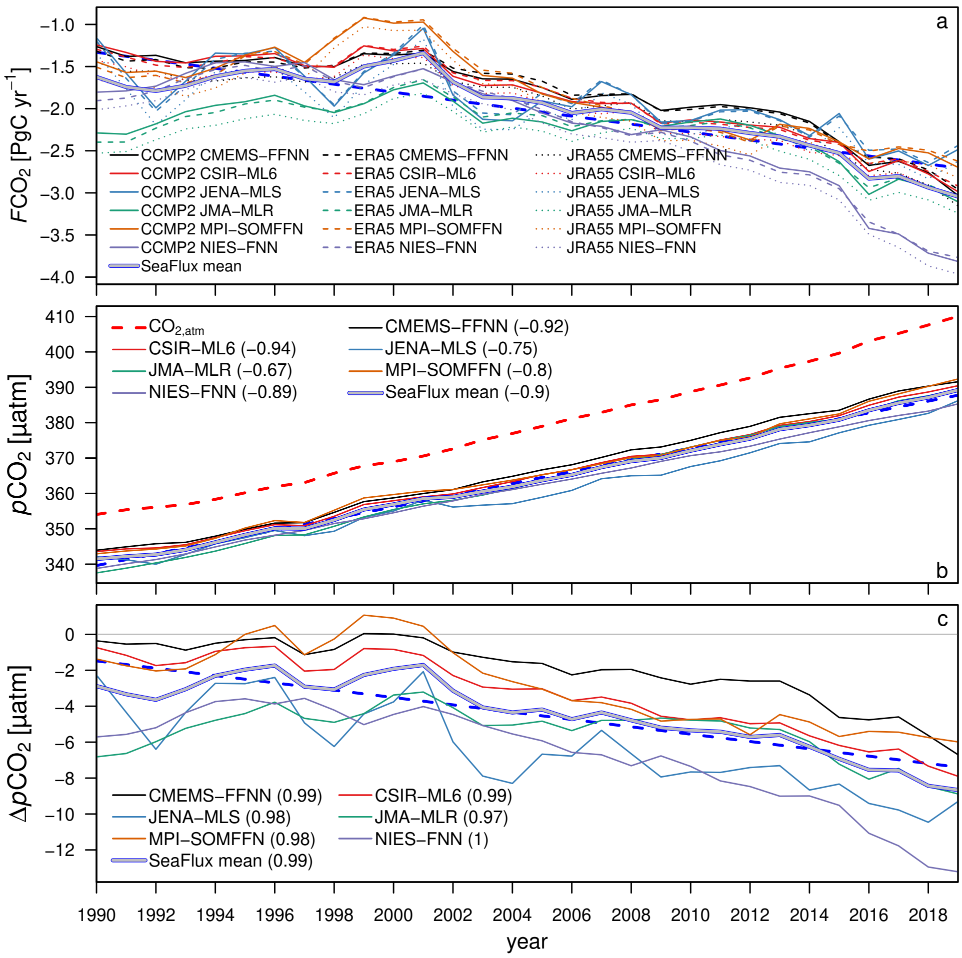

Fig. 1: Annual mean globally integrated FCO_2 (a) and averaged pCO_2 (b) and ΔpCO_2 (c) from SeaFlux (Gregor and Fay, 2021, thick gray-blue line is ensemble mean, thick dashed blue line is linear trend of ensemble mean). In a, negative values denote oceanic CO_2 uptake and labels refer to wind and pCO_2-products. In b, the red dashed line is the globally averaged observed atmospheric CO_2 mole fraction (in ppm; Lan et al, 2023). Numbers in labels in b and c provide significant correlations with a (averaged over three wind products).

The globally integrated ocean CO_2 sink is subject to a pronounced temporal variability, here identified as the annual time series minus its linear trend (Fig. 2a; negative values indicate an ocean CO_2 sink greater than suggested by its linear trend; see section 2.1). From 1990 to 2001 the SeaFlux ensemble mean FCO_2 weakens by ~0.8

PgC yr^{-1} with respect to the linear trend. Around 2000, the oceanic CO_2 uptake is lower by ∼0.5 PgC yr^{-1} than the linear trend would suggest. Thereafter, this weakening stops, the CO_2 uptake increases and follows its linear trend with a small temporal variability until ∼2013. Then, the ocean CO_2 uptake intensifies until the end of the time series (2019), eventually being ∼0.3 PgC yr^{-1} larger than its linear trend. As for absolute values, differences between detrended $F\mathrm{CO}_2$ realizations arise due to the utilized $p\mathrm{CO}_2$ as lines of different wind but identical $p\mathrm{CO}_2$ are generally clustered. Interannual $F\mathrm{CO}_2$ variability derived from the $p\mathrm{CO}_2$-products JENA-MLS (blue) and MPI-SOMFFN (orange) show the largest deviations from the ensemble mean. The absolute $F\mathrm{CO}_2$ (Fig. 1a) varies around its linear trend by about ±27% ($F\mathrm{CO}_2$/trend − 1 ranges from −27.6% to +26.5%; Gruber et al (2023) report ±20% for the same data product and time period).

The globally averaged SeaFlux $p\mathrm{CO}_2$ exhibits a concurrent temporal variability as $F\mathrm{CO}_2$ (Fig. 2b). For example, the decreasing oceanic CO_2 uptake around 1995 and 2000 co-occurs with anomalously large oceanic $p\mathrm{CO}_2$. Afterwards, the $p\mathrm{CO}_2$ variability is reduced, similarly as for $F\mathrm{CO}_2$. Finally, from ∼2015 onward, $p\mathrm{CO}_2$ continues to increase stronger than its linear trend, concurrently with a larger CO_2 uptake. $p\mathrm{CO}_2$ realizations differ from the ensemble mean in a similar way as for $F\mathrm{CO}_2$; JENA-MLS and MPI-SOMFFN show the largest deviation from the ensemble mean. The correlations between detrended $F\mathrm{CO}_2$ and detrended $p\mathrm{CO}_2$ generally decrease compared to the absolute time series in Fig. 1b (numbers in labels in Fig. 2b; e.g. −0.32 for the ensemble mean, i.e. detrended $p\mathrm{CO}_2$ explains only ∼10% of the temporal variability of detrended $F\mathrm{CO}_2$ compared to the 81% of the absolute values). In addition, the detrended time series are grouped into positive (JENA-MLS, MPI-SOMFFN), negative (CMEMS-FFNN, CSIR-ML6, ensemble mean and median) and insignificant (JMA-MLR, NIES-FNN) correlations of detrended $p\mathrm{CO}_2$ and detrended $F\mathrm{CO}_2$. The

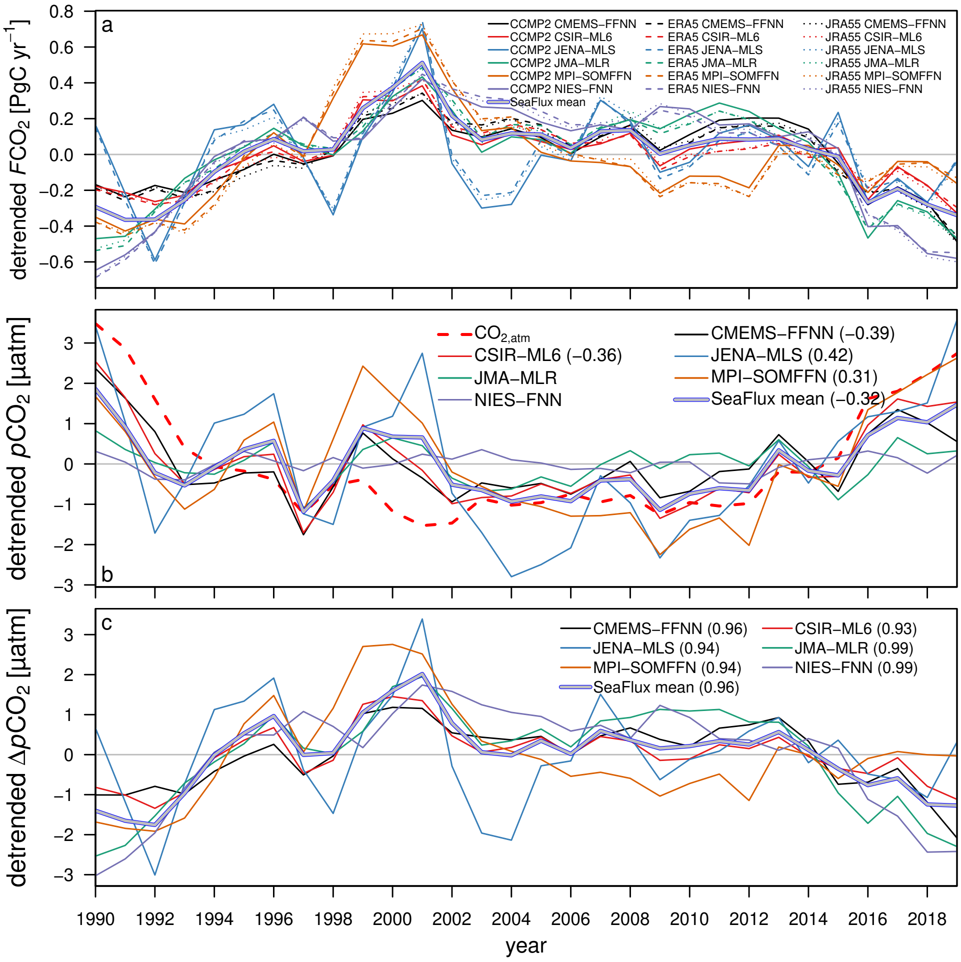

Fig. 2: As Fig. 1 but detrended annual mean globally integrated FCO_2 (a) and averaged pCO_2 (b) and ΔpCO_2 (c) from SeaFlux (Gregor and Fay, 2021, thick gray-blue line is ensemble mean). Positive values mark years of a weaker ocean CO_2 sink and higher pCO_2 or ΔpCO_2 compared to their linear trend. Labels refer to wind (FCO_2 only) and pCO_2-products. In b, the red dashed line is the globally averaged detrended observed atmospheric CO_2 mole fraction (in ppm; Lan et al, 2023). Numbers in labels in b and c provide correlations with a (averaged over three wind products), if significant.

corresponding detrended ΔpCO_2, in contrast, exhibits large correlations ≥ 0.93 with detrended FCO_2, similarly as for their absolute values (Fig. 1c).

Multi-linear regression with 21 predictors (Tab. 1) confirms that $\Delta p\mathrm{CO}_2 = p\mathrm{CO}_2 - p\mathrm{CO}_{2,\mathrm{atm}}$ is the most important predictor of interannual $F\mathrm{CO}_2$ variability (Fig. 3). Both tested information criteria $\mathrm{AIC_c}$ and BIC yield statistically indistinguishable best models based on the predictors $\Delta p\mathrm{CO}_2$, $p\mathrm{CO}_2$ and near-surface wind speed W, if combinations of significantly correlated predictors are excluded (black and red lines in Fig. 3). From these, the model with the lowest number of predictors should be selected (Burnham and Anderson, 1998; Zuur et al, 2007). Hence, out of 21 predictors, only $\Delta p\mathrm{CO}_2$ and $p\mathrm{CO}_2$ remain for both IC (red lines in Fig. 3). If, in contrast, all possibly collinear predictors are included, near-surface wind speed remains to be an important factor (also to the power of 2 and 3, but not 4) for both IC (blue dashed lines in Fig. 3). For BIC, the additional predictors Niño 3.4 anomaly index, $\mathrm{MLD}_{0.125}$, southern hemisphere sea ice extent and SST further increase the correlation with the predictand time series. However, these models are not considered further due to potential overfitting (Burnham and Anderson, 1998; Zuur et al, 2007; Dziak et al, 2019). Instead, since $p\mathrm{CO}_{2,\mathrm{atm}}$ of SeaFlux (Gregor and Fay, 2021) and the CO_2 forcing of CMIP6 models (O'Neill et al, 2016; Meinshausen et al, 2017) are very similar and well known (Lan et al, 2023), we henceforth focus on the origin of $p\mathrm{CO}_2$ discrepancies between ESMs and SeaFlux.

Turning to ESMs, CMIP6 models reproduce the long-term trend of a strengthening ocean CO_2 uptake, albeit being weaker compared to SeaFlux (black and blue dashed lines in Fig. 4a; centered $F\mathrm{CO}_2$ is shown, i.e. its temporal mean removed). The modeled temporal variability, however, is generally lower compared to the SeaFlux ensemble mean (thick black versus gray-blue lines in Fig. 4a, b). For example, the weakening ocean CO_2 sink in the mid 1990s and around 2000 that is seen in the $p\mathrm{CO}_2$-product is nearly absent in ESMs, as well as the strengthening after $\sim$2013. Likewise, the $p\mathrm{CO}_2$ increase that is larger than its linear trend around 1995 and 2000 is absent in the coupled climate models (Fig. 4c). In the early 1990s and after 2016, however,

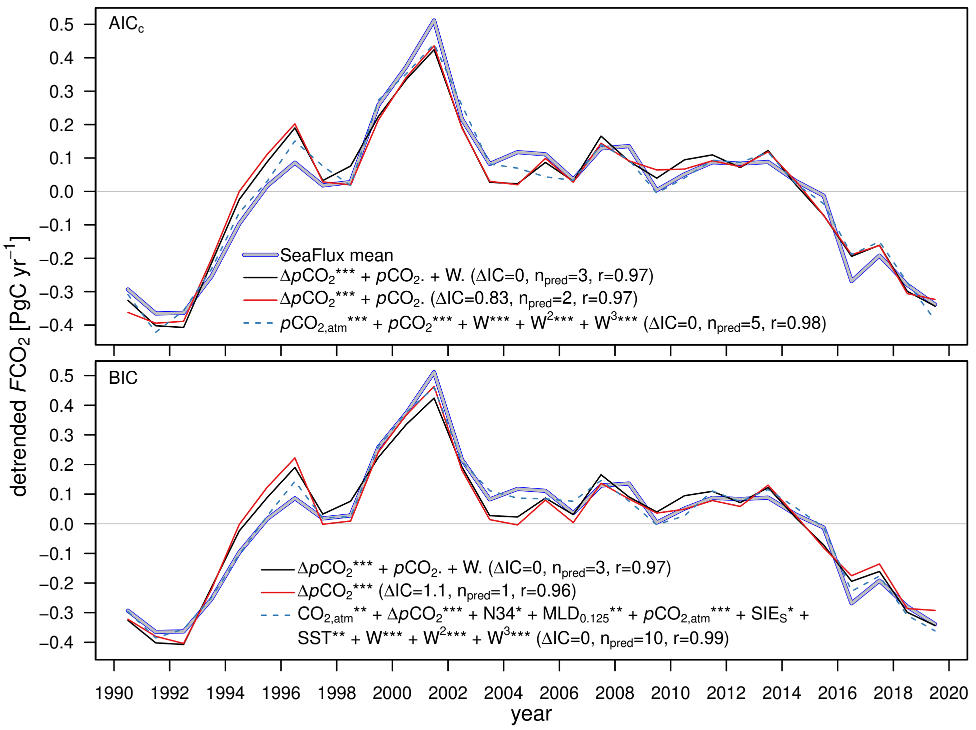

Fig. 3: Multi-linear regression of detrended annual mean globally integrated SeaFlux ensemble mean $F\text{CO}_2$ (thick gray-blue line, Gregor and Fay, 2021) based on n_{pred} = 21 predictors (Tab. 1). Black and red lines show best regression results without combinations of significantly correlated ($r > 0.5$ with $p < 0.05$) predictors according to 2 constraints: 1) minimum ΔIC (black) and, in addition, 2) minimum n_{pred} (red) for AIC$_c$ (top) and BIC (bottom). If all possibly collinear predictors are included, both constraints yield the same model for both IC, respectively (blue dashed). Labels provide predictors in alphabetical order ('+' means 'and'), their significance (.: $p <$ 0.1, *: 0.05, **: 0.01, ***: 0.001) and the correlation of the regression result with the predictand $F\text{CO}_2$.

the CMIP6 models exhibit a larger $p\text{CO}_2$ than in their linear trends, compared to the $p\text{CO}_2$-products. Correlations between modeled annual mean detrended $F\text{CO}_2$ and $p\text{CO}_2$ of individual ESMs are of similar magnitude as in the $p\text{CO}_2$-product (−0.31 to −0.4). The ensemble mean, however, reveals a larger correlation in CMIP6 (−0.52) compared to SeaFlux (−0.32). In 5 of 11 models the correlation is not significant (see labels in Fig. 4c).

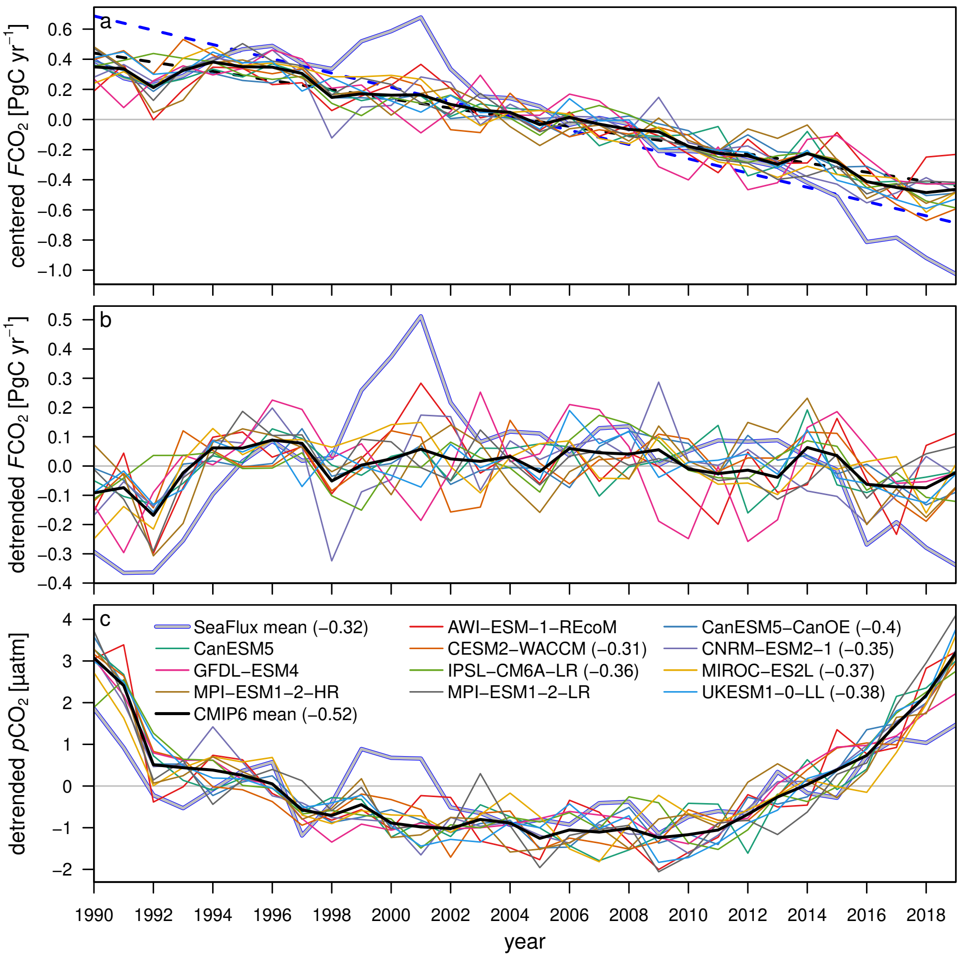

Fig. 4: Annual mean globally integrated FCO_2 (a: centered, b: detrended) and detrended globally averaged pCO_2 (c) from CMIP6 models and SeaFlux ensemble mean (Gregor and Fay, 2021). In a, thick dashed lines show linear temporal trends of ensemble means. In b and c, positive values mark years of a weaker ocean CO_2 sink and higher pCO_2 compared to their linear trend. Numbers in labels in c provide correlations between b and c, if significant.

3.2 Origin of temporal $p\mathbf{CO_2}$ variability

In the following, the discrepancy of pCO_2 variability between CMIP6 models and SeaFlux is explored. Fig. 5 shows annual mean detrended pCO_2 averaged globally and over five super-biomes (Gregor et al, 2019). Note that the pCO_2 time period is extended to 1982-2019 compared to previously shown FCO_2, as given by the SeaFlux data set. The global temporal pCO_2 variability is strongly connected to the detrended annual and global mean atmospheric CO_2 concentration $CO_{2,atm}$ (Lan et al, 2023), as detrended pCO_2 and $CO_{2,atm}$ exhibit high correlations of 0.87 and 0.98 in both the SeaFlux and CMIP6 ensemble means ('C:' numbers in labels in Fig. 5). This is especially the case in the subtropics, visible by very similar temporal pCO_2 variability from SeaFlux and ESMs (Fig. 5d, f).

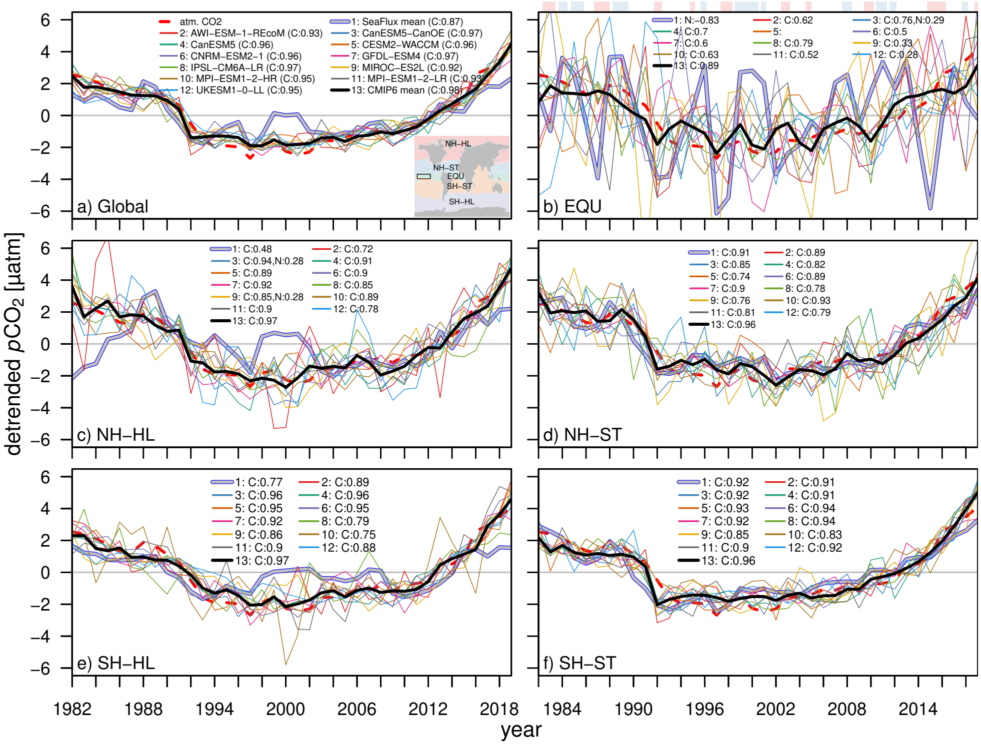

Fig. 5: Detrended annual mean pCO_2 from SeaFlux ensemble mean (Gregor and Fay, 2021) and CMIP6 models averaged globally (a) and over five biomes (map in a; Gregor et al, 2019). Positive values mark years with higher pCO_2 compared to the linear trend. Numbers in labels after 'C:' and 'N:' provide correlations with detrended annual global mean atmospheric CO_2 concentration (dashed red line identical in all panels, Lan et al, 2023) and annual mean Niño 3.4 anomaly index (Rayner, 2003), if significant. In b, red/blue bars mark El Niño/La Niña events (Niño 3.4 index area shown by black box in map).

In the high latitudes, in contrast, correlations between $CO_{2,atm}$ and pCO_2 are lower in SeaFlux (0.48 in NH-HL, 0.77 in SH-HL) compared to the CMIP6 models (0.97 in NH-HL and SH-HL; Fig. 5c, e). In these regions, similar pCO_2 discrepancies exist as for the global mean, especially for modeled pCO_2 that is lower than SeaFlux in the mid-1990s in NH-HL and around 2000 in NH-HL and SH-HL, and higher after ∼2016 in both hemispheres. In NH-HL, in addition, SeaFlux exhibits a phase of increasing pCO_2 faster than the temporal trend before 1990, while the CMIP6 models show the opposite (Fig. 5c).

In the equatorial region, SeaFlux pCO_2 and $CO_{2,atm}$ are not significantly correlated, in contrast to all other biomes (Fig. 5b). Instead, the correlation with the annual mean Niño 3.4 anomaly index is large (−0.83; Rayner, 2003). In the CMIP6 models, this situation is reversed. The model ensemble exhibits a large correlation with $CO_{2,atm}$, as in all other biomes (0.89; correlations of individual models are generally lower; CESM2-WACCM is the only model that is not significantly correlated with $CO_{2,atm}$ in EQU). Moreover, no significant correlation exists between the Niño 3.4 anomaly index and the CMIP6 ensemble average. Here, CanESM5-CanOE is the only model that exhibits a significant but small and positive correlation of 0.29 (this model as well as MIROC-ES2L additionally show significant but small correlations with the Niño 3.4 anomaly index in NH-HL; Fig. 5c). Hence, in EQU the temporal pCO_2 variability is strongly underestimated in the CMIP6 ensemble mean compared to SeaFlux. Individual models, however, do show an enhanced temporal variability.

Given the large discrepancies of temporal pCO_2 variability between the SeaFlux and CMIP6 models in the equatorial region and high latitudes, those regions will be investigated further in the remainder of this section and discussed in section 4.

3.2.1 Equatorial region

Equatorial surface pCO_2 was often shown to be determined by upwelling dynamics associated with the El Niño Southern Oscillation (ENSO). During El Niño events, trade winds weaken and the corresponding upwelling of cold and carbon-rich waters reduces. The decreasing pCO_2 leads to a reduced CO_2 outgassing or even uptake in EQU. Due to their robust anti-correlation, SST is often used as a proxy for pCO_2 variability associated with this upwelling mechanism (Boutin et al, 1999; Feely et al, 2006; Sutton et al, 2014; Liao et al, 2020). While the ESMs exhibit large ENSO-like temporal pCO_2 variability in EQU compared other biomes (Fig. 5b), a large discrepancy between the CMIP6 and SeaFlux ensemble means is reflected in the anti-correlation (-0.3) of centered (1981-2010 mean removed) SST in the Niño 3.4 index area between ESMs and observations (Fig. 6a; Rayner, 2003). Individual models are usually not correlated with observed SST or are anti-correlated (CanESM5-CanOE and CNRM-ESM2-1; numbers in labels in Fig. 6a).

In addition, the number of modeled El Niño events in this 38-year period is lower in the model ensemble mean compared to observations (6 versus 10; 12 versus 10 La Niña events), and the CMIP6 ensemble mean has a longer period of maximum SST variability (7.6 versus 5.43 years; Fig. 6b; see section 2.4). Individual models do reproduce El Niño (9 to 14 in 38 years) and La Niña (9 to 19) events similar to the SST data set. However, most models exhibit a shorter period of maximum SST variability (around 4 years).

3.2.2 High latitudes

Compared to EQU, the temporal SST variability is smaller in the high latitudes in ESMs and the two SST data sets EN4.2.2 and OISSTv2 (Fig. 7a, b; Good et al, 2013; Huang et al, 2021). Instead, the NH-HL are dominated by a significant warming trend of 0.18 ± 0.015 (EN4.2.2) or 0.2 ± 0.013 (OISSTv2) $°C\ decade^{-1}$, similarly represented in the model ensemble mean ($0.24\pm0.008\ °C\ decade^{-1}$). Anomalies around these trends are highly correlated between the two data sets and ESM ensemble mean (0.9 and 0.94). SST signals are less clear in SH-HL as the CMIP6 ensemble mean SST anomalies are not significantly correlated with EN4.2.2 but with OISSTv2 (0.79). While the ESM

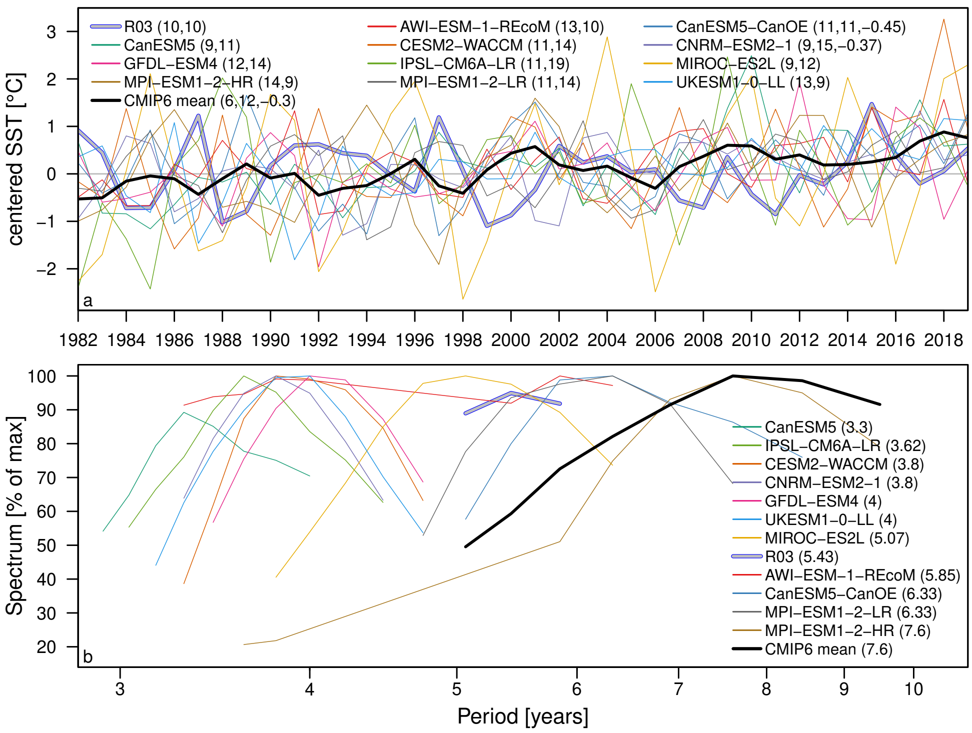

Fig. 6: a) Annual mean centered (1981-2010 mean removed) SST averaged over Niño 3.4 index area in CMIP6 models and SST data set (R03, Rayner, 2003). Numbers in labels provide El Niño and La Niña count, and, for the models, their correlation with the SST data set, if significant. b) Frequency spectra of a, scaled by individual maximum. Only values above the 80% percentile of red noise are shown. Labels are ordered by increasing period of maximum spectrum in years (in parentheses).

ensemble mean and OISSTv2 show warming trends (0.11 ± 0.005 and 0.0641 ± 0.008 °C decade^{-1}), EN4.2.2 exhibits a weak cooling trend of -0.02 ± 0.011 °C decade^{-1}.

Opposite temporal trends are seen in modeled and observation-derived $MLD_{0.03}$ anomalies in the high latitudes in both hemispheres. While EN4.2.2 indicates a $MLD_{0.03}$ deepening from 1982 to 2019, $MLD_{0.03}$ tends to shallow in all ESMs (Fig. 7c, d; positive values indicate a mixed layer deeper than the temporal mean; see section 2.4 for derivation of $MLD_{0.03}$ from EN4.2.2). In particular, the EN4.2.2 mixed layer deepening accelerates around the year 2000 in NH-HL and around 2004 in SH-HL,

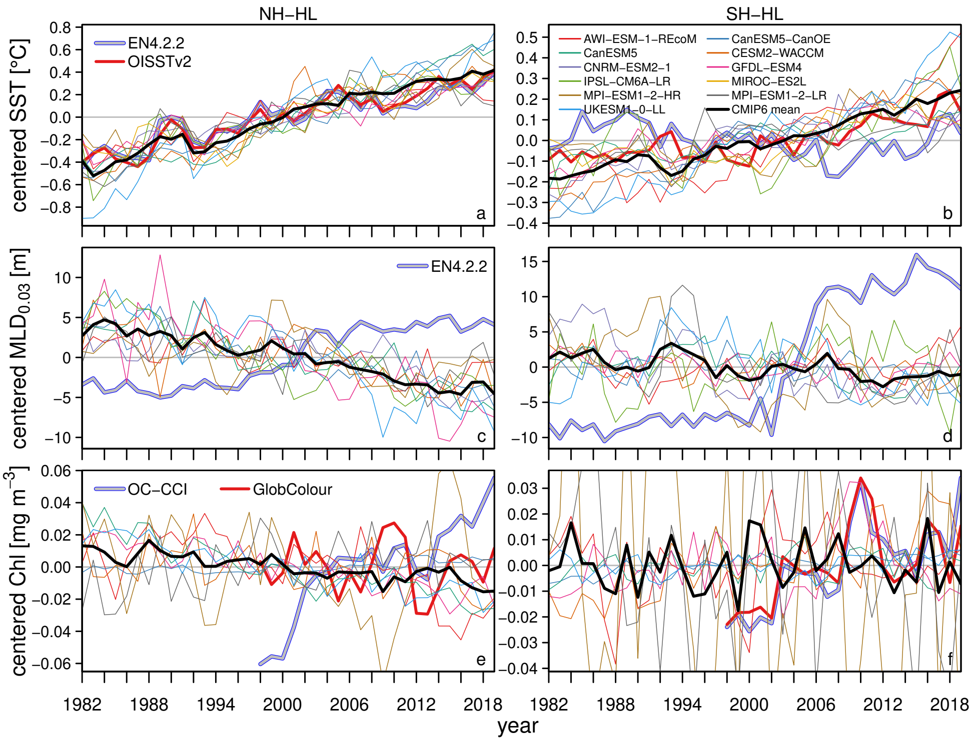

Fig. 7: Annual mean centered (1982-2019 mean removed) SST (top), $MLD_{0.03}$ (middle) and Chl (bottom) from observational data sets and CMIP6 models, spatially averaged over NH-HL (left) and SH-HL biomes (right; areas are shown in Fig. 5a). Positive values indicate values larger than the temporal mean (deeper for $MLD_{0.03}$). Data sets are OISSTv2 (Huang et al, 2021) for SST, EN4.2.2 (Good et al, 2013) for SST and $MLD_{0.03}$ (see section 2.4) and OC-CCI (Sathyendranath et al, 2019) and GlobColour (European Union-Copernicus Marine Service, 2022) for Chl. Some variables are not available for all models. In e and f, MPI-ESM values are not included in y-axes limits.

concurrently with large discrepancies in $p\mathrm{CO}_2$ variability between models and SeaFlux in these regions (Fig. 5c, e).

Surface chlorophyll (Chl) data sets are only available from 1998 (Fig. 7e, f). In NH-HL, modeled Chl anomalies are significantly anti-correlated with OC-CCI (−0.72; Sathyendranath et al, 2019) but not correlated with GlobColour (European Union-Copernicus Marine Service, 2022). The ESM ensemble mean exhibits a small decreasing Chl trend of -0.006 ± 0.0007 mg m^{-3} decade^{-1}, while Chl from OC-CCI is increasing over time (0.04±0.005 mg m^{-3} $decade^{-1}$). GlobColour does not show a significant temporal trend. The two data sets indicate different periods of anomalously low/high Chl. While OC-CCI shows Chl minima around the year 2000 and maxima in the last years of the time series, these features are absent in GlobColour. Instead, a Chl maximum is seen around 2010, directly followed by a Chl minimum around 2013. The ESMs show none of those pronounced Chl anomalies (Fig. 7e). In SH-HL, the two data seta OC-CCI and GlobColour agree more than in NH-SH by having similar increasing Chl trends of 0.02±0.004 and 0.01±0.004 mg m^{-3} $decade^{-1}$, respectively (Fig. 7f). They also show concurrent Chl minima and maxima around the years 2000 and 2010. The ESM ensemble mean does not exhibit a significant temporal trend and the modeled Chl anomalies are not significantly correlated with the observation-derived data sets. Here, the MPI-ESM model simulations show substantially larger Chl anomalies compared to all other models, as shown earlier (Schneider et al, 2008).

3.2.3 Opposite MLD trends

The contrasting $MLD_{0.03}$ trends between ESMs and observation-based data sets in the high latitudes (Fig. 7c, d) are a robust feature across all latitudes except the equatorial region (Fig. 8). ESMs generally simulate a shallowing $MLD_{0.03}$ from the 1970s to today, while the $MLD_{0.03}$ trend data set from Sallée et al (2021) as well as post processed $MLD_{0.03}$ trends based on EN4.2.2 (Good et al, 2013, see section 2.4) show the opposite (thick red and gray-blue lines in Fig. 8). Modeled $MLD_{0.03}$ trends are largest (<-10 m $decade^{-1}$) in the sub-polar North Atlantic around ∼60°N, where GFDL-ESM4, CESM2-WACCM, AWI-ESM-1-REcoM, and MPI-ESM1-2-HR exhibit a strong and CNRM-ESM2-1 and CanESM5-CanOE a weak $MLD_{0.03}$ shallowing; as well as in the Southern Ocean, where CNRM-ESM2-1, the MPI-ESM models and GFDL-ESM4 show a strong $MLD_{0.03}$ shallowing of ~ -10 m $decade^{-1}$ at ∼60 to 70°S. Here, IPSL-CM6A-LR, UKESM1-0-LL, AWI-ESM-1-REcoM, CanESM5-CanOE and CESM2-WACCM exhibit a weak $MLD_{0.03}$ deepening. Hence, $MLD_{0.03}$ trend signs generally agree between ESMs in NH-HL (with the exception of small deepening trends in GFDL-ESM4 and UKESM1-0-LL at ∼75°N) but are less obvious in SH-HL. In addition, $MLD_{0.03}$ trends from Sallée et al (2021) and EN4.2.2 show the largest discrepancies in SH-HL, while they largely agree at all other latitudes.

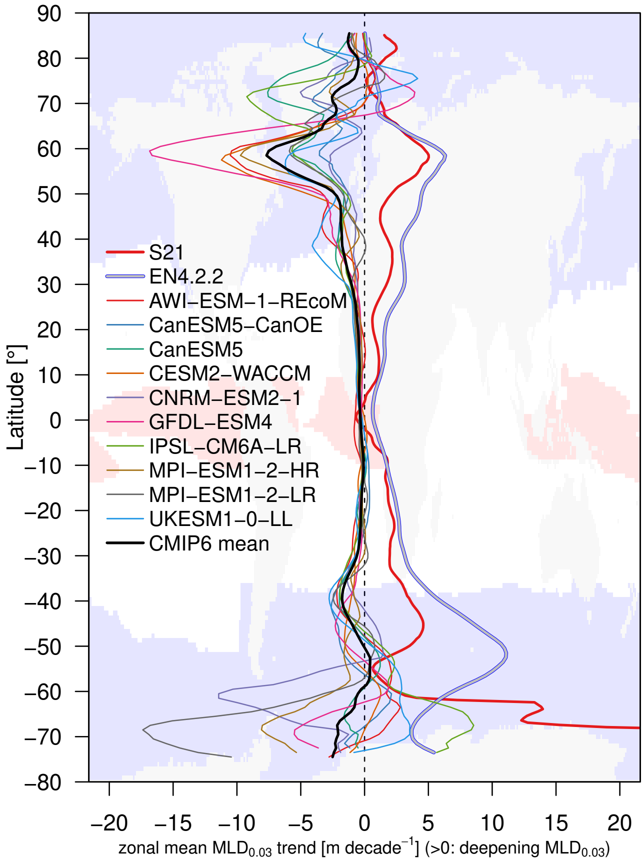

Fig. 8: Zonal mean of annual mean $MLD_{0.03}$ trend from 1970 to 2018 from data products (red: Sallée et al (2021); gray-blue: based on EN4.2.2 from Good et al, 2013, see section 2.4) and CMIP6 models. Positive values indicate a $MLD_{0.03}$ deepening. Only significant trends are included (absolute trend larger than standard error of linear regression). A running mean of 9° latitude was applied for smoothing and the latitudinal distribution of biomes (Gregor et al, 2019) is shown in the background.

The discrepancy between $MLD_{0.03}$ trends from observation-based data sets and ESMs originates from different upper ocean hydrography trends. In all biomes, and hence globally, potential density ρ^θ decreases throughout the water column from the 1970s to today, yielding lighter sea water (negative values in Fig. 9). This ρ^θ decrease generally results from increasing potential temperature θ (despite areas and/or depths of increasing practical salinity S_P; Fig. A1 and A2), is larger close to the sea surface than at depth, and, in particular, substantially stronger in ESMs compared to the EN4.2.2 data product (thick gray-blue line in Fig. 9). Since ρ^θ generally increases with depth, this depth dependence of the ρ^θ trend yields flatter density profiles and hence a shallower mixed layer. In EN4.2.2, this depth dependence of the ρ^θ trend is much weaker, yielding a near-constant shift towards lighter ρ^θ throughout the water column globally (Fig. 9a). In SH-HL, the depth dependence of the ρ^θ trend is reversed and the density decrease is weakest at the surface, consistent with a large $\mathrm{MLD}_{0.03}$ deepening in the data sets (Fig. 9e and Fig. 8). CanESM5, CESM2-WACCM and UKESM1-0-LL exhibit the largest decreasing ρ^θ trends at global scale (Fig. 9a). In NH-HL, IPSL-CM6A-LR additionally shows a large decreasing ρ^θ trend, while AWI-ESM-1-REcoM, GFDL-ESM4 and MIROC-ES2L as well as CNRM-ESM2-1 largely agree with EN4.2.2 close to the sea surface (Fig. 9c). In EQU, however, the same four models feature (small) positive ρ^θ trends between ~100 and 200 m depth, in contrast to all other models and EN4.2.2 (Fig. 9b). In SH-HL, the modeled ρ^θ trends show a reduced depth dependence compared to the other biomes, similarly as in EN4.2.2 (Fig. 9e). The weaker decreasing density trend close to the surface, however, is only captured by the two models CNRM-ESM2-1 and IPSL-CM6A-LR.

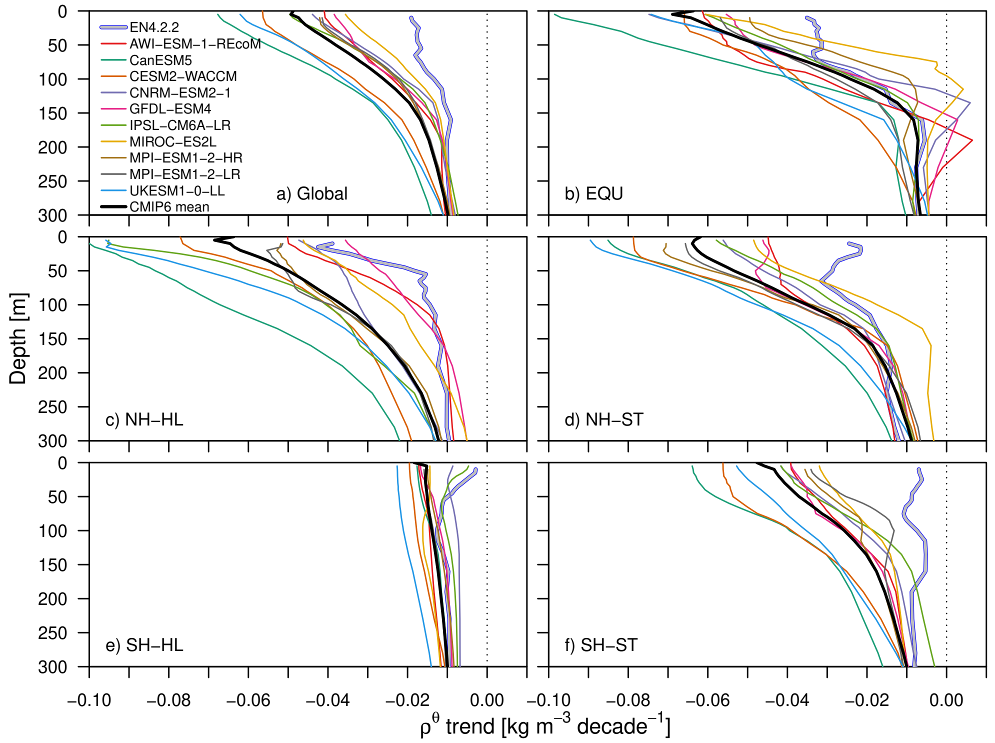

Fig. 9: Annual mean upper ocean potential density ρ^{θ} trend from 1970 to 2018 (in kg m^{-3} decade^{-1}) from CMIP6 models and a observation-based data set (EN4.2.2, Good et al, 2013) averaged globally (a) and over five biomes (b-f). Negative values denote a decreasing density. Trends of corresponding potential temperature θ and practical salinity S_P are shown in Fig. A1 and A2.

4 Discussion

4.1 Temporal FCO_2 trend and variability mostly explained by $CO_{2,atm}$

On a global scale, the air-sea CO_2 partial pressure difference $\Delta pCO_2 = pCO_2 - pCO_{2,atm}$ explains more than 92% of the temporal FCO_2 variability (here obtained by removing the linear temporal trend; e.g., DeVries, 2022, see section 2.1). Other physical variables do increase the correlation, however, to a negligible degree, as inferred by multi-linear regression with 21 predictors (Fig. 3,

Tab. 1). Since the atmospheric CO_2 concentration $CO_{2,atm}$ and sea level pressure (and hence $pCO_{2,atm}$) are relatively well known, it is crucial to understand temporal pCO_2 variability discrepancies between pCO_2-products and Earth System models, an important tool to estimate the future ocean carbon sink in our changing climate (Arora et al, 2020; Friedlingstein et al, 2022).

In the analyzed 38-year long period from 1982 to 2019 the surface ocean pCO_2 from SeaFlux (Gregor and Fay, 2021) is characterized by a significant positive trend (Fig. 1b) that is set by $CO_{2,atm}$ (Lan et al, 2023), superimposed by a temporal variability around this trend (Fig. 5). In line with McKinley et al (2020), this temporal pCO_2 variability is, as the trend, dominated by $CO_{2,atm}$ in all biomes except EQU (dashed red line and correlations labeled 'C:' in Fig. 5), and thus explains the slowdown and reinvigoration of FCO_2 before and after 2000 to a large extent (Gruber et al, 2023). Especially in the sub-tropics, $CO_{2,atm}$ explains the temporal pCO_2 variability (more than 82%; Fig. 5d, f). In the high latitudes, the influence of $CO_{2,atm}$ on pCO_2 is weaker (23 and 59% in NH-HL and SH-HL; Fig. 5c, e). Hence, compared to the sub-tropics, other factors than $CO_{2,atm}$ additionally affect the temporal pCO_2-product variability in EQU, NH-HL and SH-HL.

These findings are in line with previous work that related pCO_2 changes to changes of environmental factors. Most prominent is the exponential sensitivity to temperature (Takahashi et al, 1993). This relationship was often used to distinguish thermal and non-thermal components of pCO_2 changes, either empirically (e.g., Takahashi et al, 2002; Landschützer et al, 2018) or analytically (Gallego et al, 2018). A key outcome of these studies is that pCO_2 variability in the sub-tropics is mainly determined by thermal effects, whereas non-thermal effects such as carbon supply/removal by the ocean circulation or biological activity dominate elsewhere. Acknowledging uncertainties and overestimated variability in observation-based pCO_2 estimates due to the limited number of observations (Gloege et al, 2021; Hauck et al, 2023), we see an equivalent dependency in form of the dominant role of $CO_{2,atm}$ in the sub-tropics (Fig. 5d, f) and a weaker and not existing dependency in the high latitudes (Fig. 5c, e) and EQU (Fig. 5b) in $p\mathrm{CO}_2$ from SeaFlux. This illustrates that atmospheric CO_2 and SST are dominant drivers of $p\mathrm{CO}_2$ changes in thermally driven biomes. The analyzed CMIP6 Earth System models have problems to capture temporal $p\mathrm{CO}_2$ variability in the non-thermally driven biomes: EQU, NH-HL and SH-HL (Fig. 5b, c and e), whereas the thermally driven sub-tropics are well simulated compared to SeaFlux (Fig. 5d, f). The origin of this discrepancy is discussed in the following.

4.2 Biased ENSO upwelling dynamics

As outlined in section 3.2.1, SST can be used as a proxy for $p\mathrm{CO}_2$ changes through upwelling in the equatorial region (e.g., McKinley et al, 2017). SST time series of individual models are generally uncorrelated with the observation-based SST data set (Rayner, 2003) and periods of maximum variability are generally too short to represent typical ENSO periods (5 to 6 years based on Rayner (2003) shown in Fig. 6; typically reported at 3-7 years, e.g., Timmermann et al, 2018). This model bias was shown earlier (Beobide-Arsuaga et al, 2021) and is of importance since the Niño 3.4 anomaly index explains ∼70% of the temporal $p\mathrm{CO}_2$ variability in this region (Fig. 5b) and is strongly correlated to equatorial $F\mathrm{CO}_2$ in the Pacific (Rödenbeck et al, 2022; Vaittinada Ayar et al, 2022) and $p\mathrm{CO}_2$ in the Atlantic (Koseki et al, 2023).

4.3 Opposite mixed layer depth trends

A striking discrepancy between observational data sets and ESMs is seen in high-latitude $\mathrm{MLD}_{0.03}$ trends (Fig. 7c, d and Fig. 8). All ESMs simulate a shallowing mixed layer over the analyzed period, in contrast to results based on EN4.2.2 (Good et al, 2013, see section 2.4) and Sallée et al (2021). The observed mixed layer deepening is largest during the 2000s in NH-HL and SH-HL (Fig. 7c, d), the same years when observation-based $p\mathrm{CO}_2$ increases, thereby deviating from the decadal variability defined by $CO_{2,atm}$, as discussed above. This concurrency suggests a significant carbon supply from depth by enhanced mixing in the high latitudes, a feature that seems to be missing in the analyzed CMIP6 models. In addition, the modeled $MLD_{0.03}$ trend bias across all latitudes except the equatorial region (Fig. 8) suggests that this carbon supply by enhanced mixing is of minor importance in the sub-tropics, as there the temporal $p CO_2$ variability from ESMs and SeaFlux largely agree due to the common $CO_{2,atm}$ forcing (Fig. 5d, f).

We note that the temporal change of $MLD_{0.03}$ based on EN4.2.2 (Fig. 7c, d) arises concurrently with a large increase of gliders and profiling floats in the data sets, especially from the Argo program (Meyssignac et al, 2019). Despite corrections in EN4.2.2 (Gouretski and Reseghetti, 2010; Gouretski and Cheng, 2020), it is not clear to us if and how an increased measurement density affects the resulting hydrographic data set (e.g., Cheng and Zhu, 2014). Sallée et al (2021), however, obtained similar $MLD_{0.03}$ deepening trends without Argo data (their Extended Data Figure 9b), thus we consider our post processed $MLD_{0.03}$ product based on EN4.2.2 as robust.

The effect of ocean ventilation on carbon dynamics is an active research question (e.g., Talley et al, 2016; DeVries et al, 2017; Keppler and Landschützer, 2019; Morrison et al, 2022; Terhaar et al, 2022). Our findings provide further evidence that intensified ocean mixing increases the upper ocean carbon content, thereby affecting $F CO_2$, as shown primarily for the Southern Ocean in observations (Wu et al, 2019; Nicholson et al, 2022; Prend et al, 2022; Chen et al, 2022) and models (Kwak et al, 2021). In addition, shallow mixed layers generally co-occur with an increased stratification in ESMs (Sallée et al, 2013), thereby inhibiting upward carbon and nutrient fluxes (Fu et al, 2016; Bourgeois et al, 2022; Fu et al, 2022). The robust inter-hemispheric MLD signal presented here suggests that this view may be generalized for the high latitudes on both hemispheres.

Concurrent with the described mixed layer dynamics, Chl satellite products indicate a relatively low biological activity around the year 2000 that could contribute to the increased pCO_2 during these years (Fig. 7e, f). Likewise, a relatively high Chl concentration in the most recent years could contribute to limit the pCO_2 increase seen in SeaFlux (Fig. 5c, e). The two data products OC-CCI (Sathyendranath et al, 2019) and GlobColour (European Union-Copernicus Marine Service, 2022) as well as the ESMs, however, show somewhat ambiguous Chl signals, why the effect of biological activity on pCO_2 variability is less clear, in line with Rödenbeck et al (2022) and Bennington et al (2022). We further speculate that the larger modeled pCO_2 in ESMs compared to SeaFlux from 2017 onwards in almost all biomes (Fig. 5) may be, at least partially, due to an overestimated atmospheric greenhouse gas forcing as utilized in the ScenarioMIP simulations. For the years 2017 to 2019, the model forcing $CO_{2,\mathrm{atm}}$ (O'Neill et al, 2016) exceeds the observations (Lan et al, 2023) by ∼0.5, ∼1 and ∼1.3 ppm, i.e. roughly half of the annual CO_2 change $\partial CO_{2,\mathrm{atm}}$, even for the experiment with the lowest radiative forcing (SSP1-1.9, not shown).

4.4 Models overestimate hydrography trends

The systematic error in modeled $\mathrm{MLD}_{0.03}$ trends originates from hydrographic model biases. Compared to EN4.2.2, the modeled upper ocean gets substantially lighter over the historical period from 1970 to 2018 (Fig. 9). Globally, an overestimated upper ocean warming and freshening is responsible for this discrepancy (Fig. A1a and A2a). In NH-HL and SH-HL, too large freshening and warming trends, respectively, lead to flatter density profiles and hence shallower mixed layers (Fig. A1c, e and A2c, e), in line with previous work (e.g., Li et al, 2020; Small et al, 2020; Sallée et al, 2021). Note that we could not identify a significant relationship between $\mathrm{MLD}_{0.03}$ trends and near-surface wind speed trends in any biome or season, for neither wind data from ERA5

(Copernicus Climate Change Service, 2019) nor modeled by ESMs (not shown), in contrast to Keppler and Landschützer (2019).

Since all analyzed CMIP6 models exhibit similar biases in how the upper ocean hydrography is affected by climate change, we grouped the ESM ensemble according to important ocean model parameters, namely the utilized vertical tracer parameterization (Fig. A3) as well as its globally averaged horizontal resolution (Fig. A4). Note that for horizontal tracer diffusion and stirring (almost) all ocean models employ the same parameterization (Tab. 2). The vertical tracer parameterization has a strong effect on the modeled upper ocean potential temperature θ trend. In all biomes, KPP- and TKE-models simulate a stronger warming (TKE-models especially in NH-HL) compared to to PP- and other models (Fig. A3). This is in line with Pan et al (2023), who show that TKE-models, i.e. ESMs that utilize the NEMO model for the ocean, exhibit a larger warming and stronger MLD response through climate change, compared to non-NEMO models. The horizontal resolution of the ocean model component, in contrast, does not show a systematic pattern of over- or underestimated θ trends, as low- and high-resolution models (here defined by the 25 and 75% quantiles of all models) are typically closer to each other compared to medium-resolution models (i.e. all other models, Fig. A4). Moreover, when extending the CMIP6 model ensemble to 59 ESMs that provide θ for the historical experiment, the horizontal ocean model resolution does not seem to have any influence on the modeled upper ocean θ trends (Fig. A6). One exception is a smaller θ trend in NH-HL modeled by high-resolution models, thereby being closer to EN4.2.2 in the upper $\sim$100 m (Fig. A6c). Similarly, the effect of the vertical tracer parameterization on the modeled θ trend is less clear if 59 CMIP6 models are compared (Fig. A5). This ad-hoc ESM grouping is not meant to be complete, but may serve as a starting point for further in-depth analyses to understand model biases in the complex interplay of the large scale ocean circulation, small scale mixing, and associated biogeochemical tracer fluxes (e.g., Löptien and Dietze, 2019; Small et al, 2020; Ellison et al, 2023).

5 Summary and Conclusion

The temporal FCO_2 trend and variability are set, to a first order, by $CO_{2,\mathrm{atm}}$ (this study; McKinley et al, 2020), and state-of-the-art ESMs were shown to be a valuable tool to represent historical seawater pCO_2 and FCO_2 variability on global and decadal scales. Superimposed are dynamics on basin and interannual scales which are, however, systematically misrepresented in CMIP6 models. First, although ESMs do exhibit an enhanced ENSO-like SST variability in the equatorial region, the associated upwelling of cold carbon-rich water appears biased since the modeled equatorial SST is generally not correlated with observations. Second, the modeled temporal mixed layer depth trend is of opposite sign compared to two observational products in all investigated CMIP6 models and across all latitudes, with the largest discrepancies in the high latitudes in both hemispheres. Vertical carbon fluxes in or across the mixed layer and thus the modeled seawater pCO_2 variability are, in consequence, suppressed and/or out-of-phase, in line with previous model work (Fu et al, 2016; Bourgeois et al, 2022; Fu et al, 2022).

To conclude, by acknowledging uncertainties in pCO_2-products (Gloege et al, 2021; Hauck et al, 2023), our comprehensive multi-model analysis highlights the importance of circulation driven pCO_2 changes for temporal FCO_2 variability in the equatorial region and high latitudes (e.g., DeVries, 2022). Since contemporary (Landschützer et al, 2018; Friedlingstein et al, 2022; Gruber et al, 2023) and likely future (Gooya et al, 2023) oceanic CO_2 uptake and release mainly occurs in these dynamically controlled regions, the systematic equatorial SST and high-latitude mixed layer depth biases in CMIP6 models identified here render FCO_2 estimates for the coming decades questionable. The wrong sign of temporal MLD trends in particular may yield unrealistic

FCO_2 mean states over time and hence misleading future carbon budgets. Hence, development of geophysical models should focus on the improvement of tracer advection and mixing within and at the interface of the oceanic mixed layer, as increasing the horizontal ocean model resolution does not seem to resolve the model deficiencies identified here.

Acknowledgments. This work used resources of the Deutsches Klimarechenzentrum (DKRZ) granted by its Scientific Steering Committee (WLA) under project ID ba1103. Funding was provided by the Initiative and Networking Fund of the Helmholtz Association (Helmholtz Young Investigator Group Marine Carbon and Ecosystem Feedbacks in the Earth System [MarESys], Grant VH-NG-1301) and by the ERC-2022-STG OceanPeak (Grant 101077209).

Appendix A Potential temperature trend bias of 59 CMIP6 models

Tab. A1 provides details of an extended ESM ensemble of 59 models for which temporal trends of upper ocean potential temperature θ were calculated from 1970 to 2014. This increased number of models renders the θ trend differences between ESM groups of distinct vertical tracer parameterizations (Fig. A3 vs. Fig. A5) and horizontal ocean model resolution (Fig. A4 vs. Fig. A6) less pronounced, especially with respect to the horizontal ocean model resolution (except in NH-HL, Fig. A6c; see section 4.4).

Table A1: As Tab. 2 but for an extended set of 59 CMIP6 models. BL79: Bryan and Lewis (1979), C87: Cox (1987), Canuto: Canuto et al (2001, 2002), EPBL: Reichl and Hallberg (2018), FFH: mixed layer eddies as in Fox-Kemper et al (2011), G95: Gent et al (1995), GM90: Gent and Mcwilliams (1990), KPP: Large et al (1994), MD98: McDougall and Dewar (1998), MY25: Mellor and Yamada (1982), NK99: Noh and Jin Kim (1999), PP: Pacanowski and Philander (1981), R82: Redi (1982), TKE: Gaspar et al (1990), UB03: Umlauf and Burchard (2003).

No	ESM	Ocean model	$\bar{d}_{\max}$	n_{lev}	horizontal	vertical
1,2	ACCESS-{CM2,ESM1-5} (Bi et al, 2020; Ziehn et al, 2020)	MOM5.1 (Griffies, 2014)	120	50	R82, GM90	KPP, FFH
3-5	AWI-{CM-1-1,ESM-1-{1-LR,REcoM}} (Semmler et al, 2020, this study)	FESOM1.4 (Wang et al, 2014)	{33,76,76}	46	R82, G95	KPP
6,7	BCC{CSM2-MR,ESM1} (Wu et al, 2019, 2020)	MOM4 (Griffies et al, 2005)	129	40	R82, GM90	KPP
8	CAMS-CSM1-0 (Rong, 2019)	MOM4 (Griffies et al, 2005)	133	50	R82, GM90	KPP
9,10	CanESM5{-CanOE} (Swart et al, 2019)	NEMO3.4.1 (Saenko et al, 2018)	116	{41,45}	R82, GM90	TKE
11	CAS-ESM2-0 (Li et al, 2023)	LICOM2.0 (Liu et al, 2012)	135	30	GM90	Canuto

No	ESM	Ocean model	$\overline{d}_{\max}$	n_{lev}	horizontal	vertical
12-15	CESM2{-{FV,WACCM{-FV}}} (Danabasoglu et al, 2020)	POP2 (Danabasoglu et al, 2012)	113	60	R82, GM90	KPP, FFH
16	CIESM (Lin et al, 2020)	POP2 (Danabasoglu et al, 2012)	113	60	R82, GM90	KPP, FFH
17-19	CMCC-{CM2-{HR4,SR5},ESM2} (Cherchi et al, 2019; Lovato et al, 2022)	NEMO3.6 (Cherchi et al, 2019)	{31,118,118}	50	R82, "additional eddy-induced velocity" (assume GM90)	TKE, FFH
20-22	CNRM-{CM6-1{-HR},ESM2-1} (Voldoire et al, 2019; Séférian et al, 2019)	NEMO3.6 (Danabasoglu et al, 2014; Voldoire et al, 2019)	{118,31,118}	75	R82, GM90	TKE, FFH
23-25	E3SM-1-{0,1{-ECA}} (Golaz et al, 2019)	MPAS-Ocean v6.0 (Petersen et al, 2019)	143	60	GM90	KPP
26-30	EC-Earth3{-{AerChem,CC,Veg{-LR}}} (Döscher et al, 2022)	NEMO3.6 (Döscher et al, 2022)	118	75	R82, GM90	TKE (=0 below MLD), FFH

No	ESM	Ocean model	$\overline{d}_{\max}$	n_{lev}	horizontal	vertical
31,32	FGOALS-{f3-L,g3} (Guo et al, 2020; Li et al, 2020)	LICOM3.0 (Liu et al, 2012)	134	30	R82, GM90	Canuto
33	FIO-ESM-2-0 (Bao et al, 2020)	POP2 (no ref given; assume Danabasoglu et al, 2012)	113	61	R82, GM90	KPP
34,35	GFDL-{CM4,ESM4} (Dunne et al, 2020)	GFDL-OM4 (Adcroft et al, 2019)	{31,59}	75	R82, G95	EPBL, FFH
36,37	GISS-E2-1-G{-CC} (Kelley et al, 2020)	GISS Ocean v1 (Kelley et al, 2020) based on Russel Ocean (Romanou et al, 2013; Schmidt et al, 2014)	158	32	R82, GM90	KPP
38	GISS-E2-1-H (Kelley et al, 2020)	HYCOM (Sun and Bleck, 2006; Romanou et al, 2013)	143	26	GM90 at isopycnal levels	KPP in mixed layer, MD98 below
39,40	HadGEM3-GC31-{LL,MM} (Roberts et al, 2019)	UK-GO6 (Storkey et al, 2018; Kuhlbrodt et al, 2018) based on NEMO3.6	{117,32}	75	{R82, variable (HL96) GM90; none}	TKE

No	ESM	Ocean model	$\overline{d}_{\max}$	n_{lev}	horizontal	vertical
41	ICON-ESM-LR (Jungclaus et al, 2022)	ICON-O (Jungclaus et al, 2022)	56 (40 according to ref)	40	R82, GM90	TKE
42,43	INM-CM{4-8,5-0} (Volodin et al, 2017)	INM-OM5 (Zalesny et al, 2010)	143	40	?	PP
44,45	IPSL-CM{5A2-INCA,6A-LR} (Boucher et al, 2020; Sepulchre et al, 2020)	NEMO3.6 (Boucher et al, 2020)	{368,117}	{31,75}	R82, GM90	TKE, FFH
46	MCM-UA-1-0 (Delworth et al, 2002)	MOM1 (Delworth et al, 2002)	301	18	R82, C87	BL79
47,48	MIROC{6,-ES2L} (Tatebe et al, 2019; Hajima et al, 2020)	COCO4.9 (Hasumi, 2015)	125	63	C87, GM90	NK99
49-51	MPI-ESM{-1-2-HAM,1-2-{HR,LR}} (Mauritsen et al, 2019)	MPIOM1.63 (Marsland et al, 2003; Jungclaus et al, 2013)	{180, 60, 180}	40	R82, G95	PP, wind-driven turbulent mixing in mixed layer
52	MRI-ESM2-0 (Yukimoto et al, 2019)	MRI.COMv4 (Tsujino et al, 2017)	103	61	R82, GM90	UB03

No	ESM	Ocean model	$\overline{d}_{\mathrm{max}}$	n_{lev}	horizontal	vertical
53	NESM3 (Cao et al, 2018)	NEMO3.4 (Cao et al, 2018)	118	46	R82, GM90	TKE
54	NorCPM1 (Bethke et al, 2021)	BLOM (Bentsen et al, 2013) based on MICOM (Bleck et al, 1992)	113	53	GM90 (Eden and Greatbatch, 2008)	TKE (Oberhuber, 1993), shear: KPP, FFH
55,56	NorESM2-{LM,MM} (Seland et al, 2020)	BLOM (Bentsen et al, 2013; Seland et al, 2020) based on MICOM (Bleck et al, 1992)	109	70	GM90 (Eden and Greatbatch, 2008)	TKE (Oberhuber, 1993), shear: 2nd order turbulence closure, FFH
57	SAM0-UNICON (Park et al, 2019)	POP2 (no ref given; assume Danabasoglu et al, 2012)	113	60	R82, GM90	KPP, FFH
58	TaiESM1 (Lee et al, 2020)	POP2 (Danabasoglu et al, 2012; Hurrell et al, 2013)	113	60	R82, GM90	KPP, FFH
59	UKESM1-0-LL (Sellar et al, 2019)	UK-GO6 (Storkey et al, 2018; Kuhlbrodt et al, 2018) based on NEMO3.6	117	75	R82, GM90	TKE

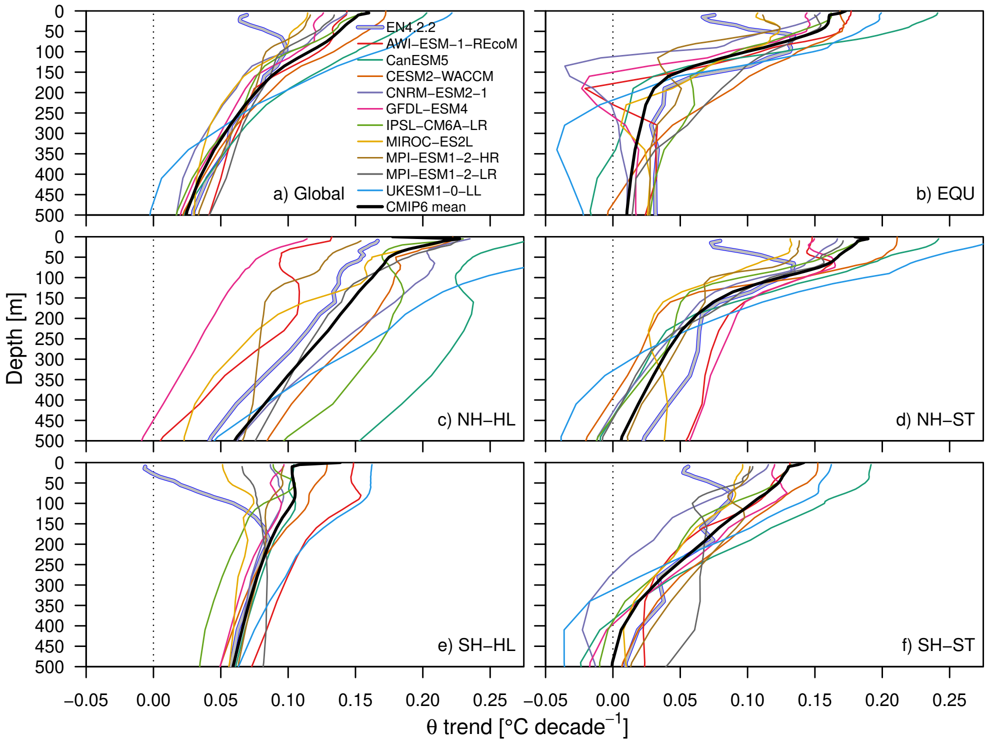

Fig. A1: As Fig. 9 but for potential temperature θ in °C decade^{-1}. Positive values denote an increasing temperature. In c, the maximum temperature trend of UKESM1-0-LL is ∼0.38 °C decade^{-1}. Fig. A3 and A4 show the same but models grouped by the vertical tracer parameterization in the mixed layer and horizontal resolution of their ocean model component.

References

Adcroft A, Anderson W, Balaji V, et al (2019) The GFDL global ocean and sea ice model OM4.0: Model description and simulation features. Journal of Advances in Modeling Earth Systems 11(10):3167–3211. https://doi.org/10.1029/2019ms001726, URL https://doi.org/10.1029/2019ms001726

Arora VK, Katavouta A, Williams RG, et al (2020) Carbon–concentration and carbon–climate feedbacks in CMIP6 models and their comparison to CMIP5 models.

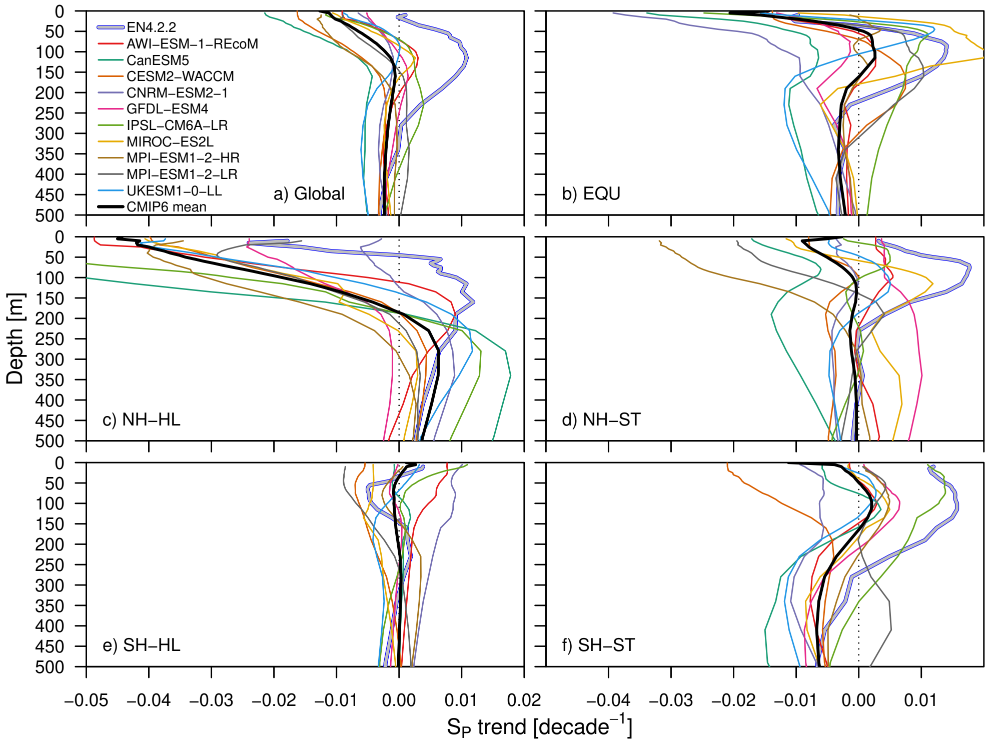

Fig. A2: As Fig. 9 but for practical salinity S_P in decade^{-1}. Negative values denote a decreasing salinity. In c, the minimum salinity trends of CanESM5 and IPSL-CM6A-LR are ~ -0.08 and ~ -0.09 decade^{-1}.

Biogeosciences 17(16):4173–4222. https://doi.org/10.5194/bg-17-4173-2020, URL https://doi.org/10.5194/bg-17-4173-2020

Atlas R, Hoffman RN, Ardizzone J, et al (2011) A cross-calibrated, multiplatform ocean surface wind velocity product for meteorological and oceanographic applications. Bulletin of the American Meteorological Society 92(2):157–174. https://doi.org/10.1175/2010bams2946.1, URL https://doi.org/10.1175/2010bams2946.1

Bakker DCE, Pfeil B, Landa CS, et al (2016) A multi-decade record of high-quality fco2 data in version 3 of the surface ocean co2 atlas (socat). Earth System Science Data 8(2):383–413. https://doi.org/10.5194/essd-8-383-2016, URL https://doi.org/10.5194/essd-8-383-2016

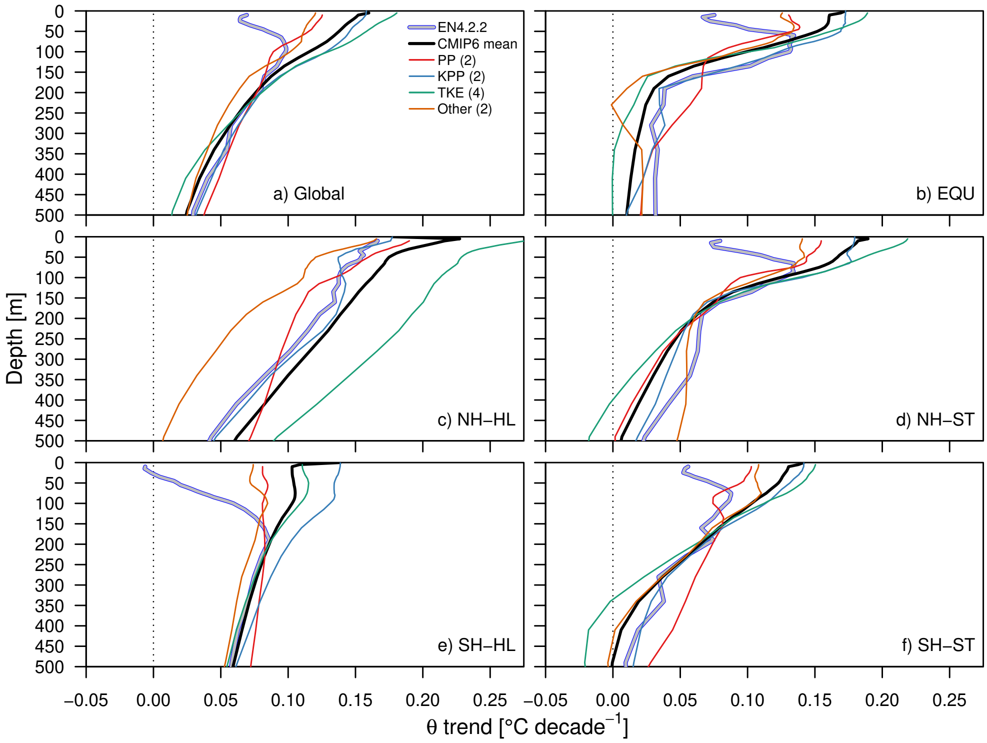

Fig. A3: As Fig. A1 but models grouped by the vertical tracer parameterization in the mixed layer of their ocean model component (Tab. 2). Fig. A5 shows the same but for an extended set of 59 CMIP6 models.

Bao Y, Song Z, Qiao F (2020) FIO-ESM version 2.0: Model description and evaluation. J Geophys Res Oceans 125(6)

Bartoń K (2022) MuMIn: Multi-Model Inference. URL https://CRAN.R-project.org/package=MuMIn, r package version 1.46.0

Bennington V, Galjanic T, McKinley GA (2022) Explicit physical knowledge in machine learning for ocean carbon flux reconstruction: The pco$_2$-residual method. Journal of Advances in Modeling Earth Systems 14(10). https://doi.org/10.1029/2021ms002960, URL https://doi.org/10.1029/2021ms002960

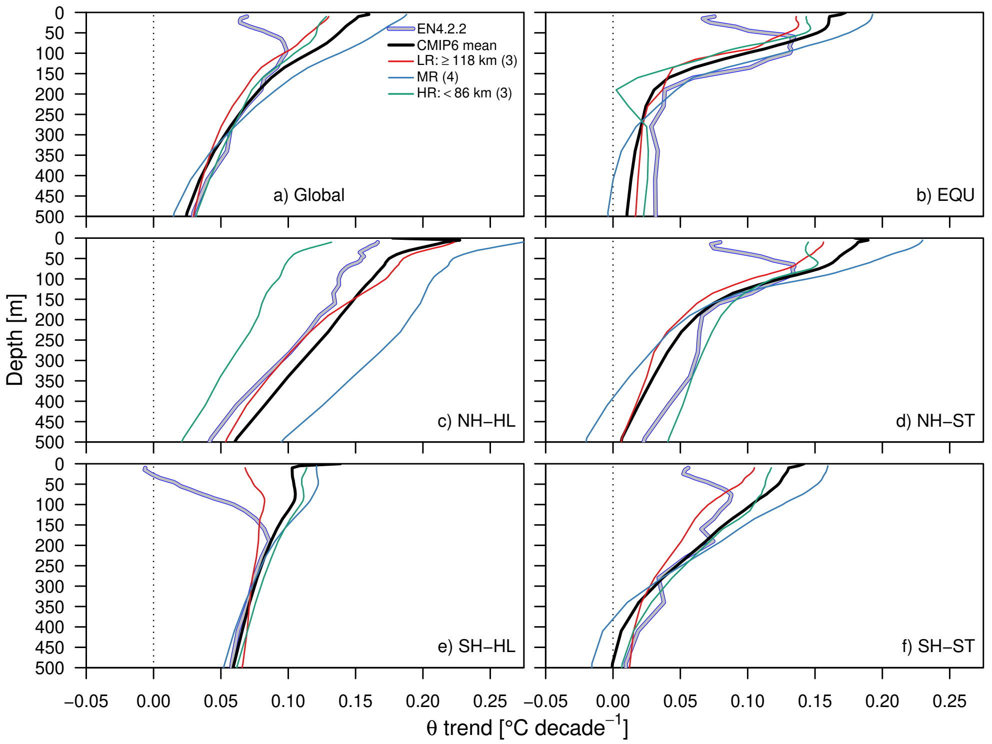

Fig. A4: As Fig. A1 but models grouped by the globally averaged horizontal resolution of the ocean model component (Tab. 2). Low and high resolution (LR, HR) models are selected by the 25 and 75% quantiles (86 and 118 km) of all resolutions (minimum and maximum are 59 and 180 km). Medium resolution (MR) models are within LR and HR (median 117 km). Fig. A6 shows the same but for an extended set of 59 CMIP6 models.

Bentsen M, Bethke I, Debernard JB, et al (2013) The norwegian earth system model, noresm1-m–part 1: description and basic evaluation of the physical climate. Geoscientific Model Development 6(3):687–720

Beobide-Arsuaga G, Bayr T, Reintges A, et al (2021) Uncertainty of enso-amplitude projections in cmip5 and cmip6 models. Climate Dynamics 56(11):3875–3888. https://doi.org/10.1007/s00382-021-05673-4, URL https://doi.org/10.1007/s00382-021-05673-4

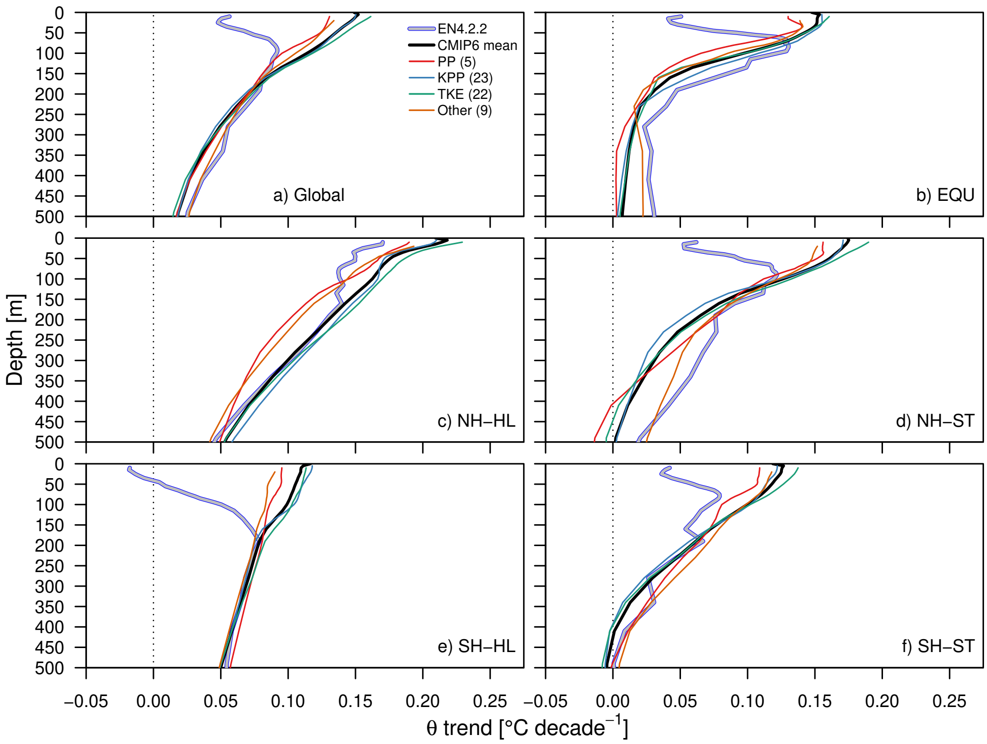

Fig. A5: As Fig. A3 but for an extended set of 59 CMIP6 models (Tab. A1) over the historical period from 1970 to 2014.

Bethke I, Wang Y, Counillon F, et al (2021) NorCPM1 and its contribution to CMIP6 DCPP. Geosci Model Dev 14(11):7073–7116

Bi D, Dix M, Marsland S, et al (2020) Configuration and spin-up of access-cm2, the new generation australian community climate and earth system simulator coupled model. Journal of Southern Hemisphere Earth Systems Science 70(1):225–251. https://doi.org/10.1071/es19040, URL http://dx.doi.org/10.1071/ES19040

Bleck R, Rooth C, Hu D, et al (1992) Salinity-driven thermocline transients in a wind- and thermohaline-forced isopycnic coordinate model of the north atlantic. Journal of Physical Oceanography 22(12):1486–1505

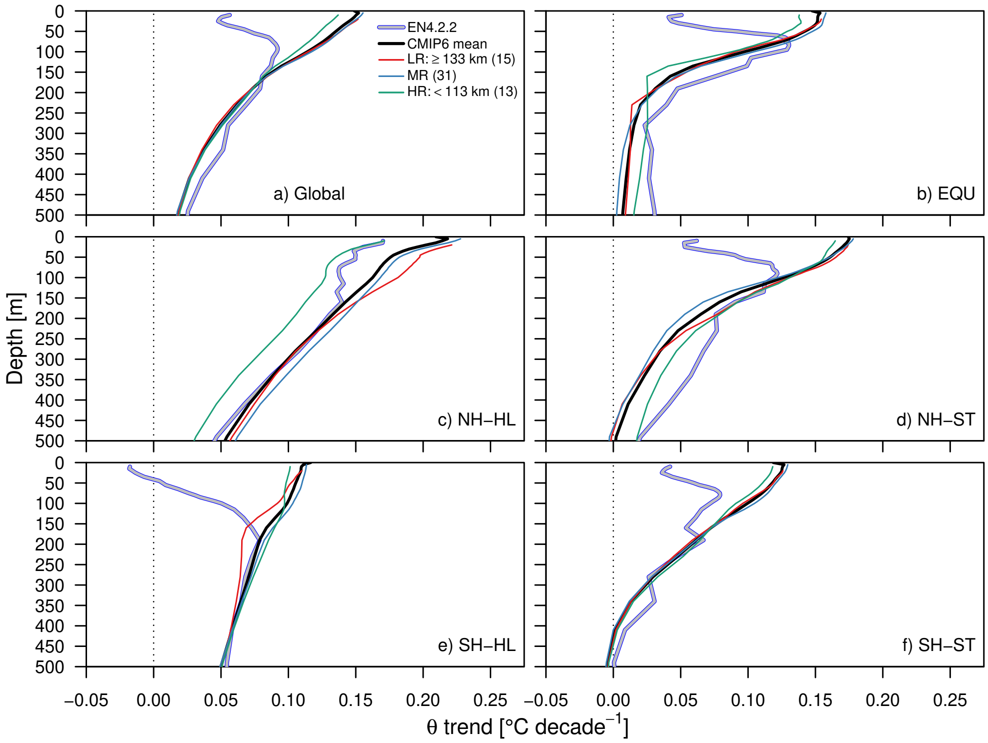

Fig. A6: As Fig. A4 but for an extended set of 59 CMIP6 models (Tab. A1) over the historical period from 1970 to 2014. The minimum, 25, 50 and 75% quantiles and maximum resolution are 31, 113, 118, 134 and 368 km.

Boucher O, Servonnat J, Albright AL, et al (2020) Presentation and evaluation of the IPSL-CM6a-LR climate model. Journal of Advances in Modeling Earth Systems 12(7). https://doi.org/10.1029/2019ms002010, URL https://doi.org/10.1029/2019ms002010

Bourgeois T, Goris N, Schwinger J, et al (2022) Stratification constrains future heat and carbon uptake in the southern ocean between 30°s and 55°s. Nature Communications 13(1). https://doi.org/10.1038/s41467-022-27979-5, URL https://doi.org/10.1038/s41467-022-27979-5

Boutin J, Etcheto J, Dandonneau Y, et al (1999) Satellite sea surface temperature: a powerful tool for interpreting in situ pco2 measurements in the equatorial pacific ocean. Tellus B 51(2):490–508. https://doi.org/10.1034/j.1600-0889.1999.00025.x, URL http://dx.doi.org/10.1034/j.1600-0889.1999.00025.x

Bryan K, Lewis LJ (1979) A water mass model of the world ocean. Journal of Geophysical Research: Oceans 84(C5):2503–2517. https://doi.org/10.1029/jc084ic05p02503, URL http://dx.doi.org/10.1029/JC084iC05p02503

Bunn A, Korpela M, Biondi F, et al (2022) dplR: Dendrochronology Program Library in R. URL https://CRAN.R-project.org/package=dplR, r package version 1.7.4

Burnham KP, Anderson DR (1998) Model Selection and Inference. Springer New York, https://doi.org/10.1007/978-1-4757-2917-7, URL https://doi.org/10.1007/978-1-4757-2917-7

Canadell J, Monteiro P, Costa M, et al (2021) Global carbon and other biogeochemical cycles and feedbacks. In: Masson-Delmotte V, Zhai P, Pirani A, et al (eds) Climate Change 2021: The Physical Science Basis. Contribution of Working Group I to the Sixth Assessment Report of the Intergovernmental Panel on Climate Change. Cambridge University Press, Cambridge, UK and New York, NY, USA, book section 5, https://doi.org/10.1017/9781009157896.007, URL https://www.ipcc.ch/report/ar6/wg1/downloads/report/IPCC_AR6_WGI_Chapter05.pdf

Canuto VM, Howard A, Cheng Y, et al (2001) Ocean turbulence. part i: One-point closure model—momentum and heat vertical diffusivities. Journal of Physical Oceanography 31(6):1413–1426. https://doi.org/10.1175/1520-0485(2001)031<1413:otpiop>2.0.co;2, URL http://dx.doi.org/10.1175/1520-0485(2001)031<1413:OTPIOP>2.0.CO;2

Canuto VM, Howard A, Cheng Y, et al (2002) Ocean turbulence. part ii: Vertical diffusivities of momentum, heat, salt, mass, and passive scalars. Journal of Physical

Oceanography 32(1):240–264. https://doi.org/10.1175/1520-0485(2002)032<0240:otpivd>2.0.co;2, URL http://dx.doi.org/10.1175/1520-0485(2002)032<0240:OTPIVD>2.0.CO;2

Cao J, Wang B, Yang YM, et al (2018) The NUIST earth system model (NESM) version 3: description and preliminary evaluation. Geosci Model Dev 11(7):2975–2993

Chen H, Haumann FA, Talley LD, et al (2022) The deep ocean's carbon exhaust. Global Biogeochemical Cycles 36(7). https://doi.org/10.1029/2021gb007156, URL https://doi.org/10.1029/2021gb007156

Cheng L, Zhu J (2014) Artifacts in variations of ocean heat content induced by the observation system changes. Geophysical Research Letters 41(20):7276–7283. https://doi.org/https://doi.org/10.1002/2014GL061881, URL https://agupubs.onlinelibrary.wiley.com/doi/abs/10.1002/2014GL061881, https://agupubs.onlinelibrary.wiley.com/doi/pdf/10.1002/2014GL061881

Cherchi A, Fogli PG, Lovato T, et al (2019) Global mean climate and main patterns of variability in the cmcc-cm2 coupled model. Journal of Advances in Modeling Earth Systems 11(1):185–209. https://doi.org/10.1029/2018ms001369, URL http://dx.doi.org/10.1029/2018MS001369

Cinquini L, Crichton D, Mattmann C, et al (2014) The earth system grid federation: An open infrastructure for access to distributed geospatial data. Future Generation Computer Systems 36:400–417. https://doi.org/10.1016/j.future.2013.07.002, URL https://doi.org/10.1016/j.future.2013.07.002

Copernicus Climate Change Service (2019) Era5 monthly averaged data on single levels from 1979 to present. https://doi.org/10.24381/CDS.F17050D7, URL https:

//cds.climate.copernicus.eu/doi/10.24381/cds.f17050d7

Cox MD (1987) Isopycnal diffusion in a z-coordinate ocean model. Ocean Modelling (unpublished manuscript) 74:1–5

Craig A, Valcke S, Coquart L (2017) Development and performance of a new version of the OASIS coupler, OASIS3-MCT_3.0. Geoscientific Model Development 10(9):3297–3308. https://doi.org/10.5194/gmd-10-3297-2017, URL https://doi.org/10.5194/gmd-10-3297-2017

Danabasoglu G, Bates SC, Briegleb BP, et al (2012) The CCSM4 ocean component. Journal of Climate 25(5):1361–1389. https://doi.org/10.1175/jcli-d-11-00091.1, URL https://doi.org/10.1175/jcli-d-11-00091.1

Danabasoglu G, Yeager SG, Bailey D, et al (2014) North atlantic simulations in coordinated ocean-ice reference experiments phase II (CORE-II). part i: Mean states. Ocean Modelling 73:76–107. https://doi.org/10.1016/j.ocemod.2013.10.005, URL https://doi.org/10.1016/j.ocemod.2013.10.005

Danabasoglu G, Lamarque JF, Bacmeister J, et al (2020) The community earth system model version 2 (CESM2). Journal of Advances in Modeling Earth Systems 12(2). https://doi.org/10.1029/2019ms001916, URL https://doi.org/10.1029/2019ms001916

Danek C, Shi X, Stepanek C, et al (2020) Awi awi-esm1.1lr model output prepared for cmip6 cmip historical. https://doi.org/10.22033/ESGF/CMIP6.9328, URL http://cera-www.dkrz.de/WDCC/meta/CMIP6/CMIP6.CMIP.AWI.AWI-ESM-1-1-LR.historical

Danilov S (2022) On the resolution of triangular meshes. Journal of Advances in Modeling Earth Systems 14(10). https://doi.org/10.1029/2022ms003177, URL https:

//doi.org/10.1029/2022ms003177

Danilov S, Kivman G, Schröter J (2004) A finite-element ocean model: principles and evaluation. Ocean Modelling 6(2):125–150. https://doi.org/10.1016/s1463-5003(02)00063-x, URL https://doi.org/10.1016/s1463-5003(02)00063-x

Delworth, Stouffer, Dixon, et al (2002) Review of simulations of climate variability and change with the GFDL R30 coupled climate model. Clim Dyn 19(7):555–574

DeVries T (2022) Atmospheric co2 and sea surface temperature variability cannot explain recent decadal variability of the ocean co2 sink. Geophysical Research Letters 49(7). https://doi.org/10.1029/2021gl096018, URL https://doi.org/10.1029/2021gl096018

DeVries T, Holzer M, Primeau F (2017) Recent increase in oceanic carbon uptake driven by weaker upper-ocean overturning. Nature 542(7640):215–218. https://doi.org/10.1038/nature21068, URL https://doi.org/10.1038/nature21068

DeVries T, Yamamoto K, Wanninkhof R, et al (2023) Magnitude, trends, and variability of the global ocean carbon sink from 1985 to 2018. Global Biogeochemical Cycles 37(10). https://doi.org/10.1029/2023gb007780, URL https://doi.org/10.1029/2023gb007780

Döscher R, Acosta M, Alessandri A, et al (2022) The ec-earth3 earth system model for the coupled model intercomparison project 6. Geoscientific Model Development 15(7):2973–3020. https://doi.org/10.5194/gmd-15-2973-2022, URL http://dx.doi.org/10.5194/gmd-15-2973-2022

Dunne JP, Horowitz LW, Adcroft AJ, et al (2020) The GFDL earth system model version 4.1 (GFDL-ESM 4.1): Overall coupled model description and simulation characteristics. Journal of Advances in Modeling Earth Systems 12(11). https://doi.

org/10.1029/2019ms002015, URL https://doi.org/10.1029/2019ms002015

Dziak JJ, Coffman DL, Lanza ST, et al (2019) Sensitivity and specificity of information criteria. Briefings in Bioinformatics 21(2):553–565. https://doi.org/10.1093/bib/bbz016, URL https://doi.org/10.1093/bib/bbz016

Eden C, Greatbatch RJ (2008) Towards a mesoscale eddy closure. Ocean Modelling 20(3):223–239

Ellison E, Cimoli L, Mashayek A (2023) Multi-time scale control of southern ocean diapycnal mixing over atlantic tracer budgets. Climate Dynamics 60(9):3039–3050. https://doi.org/10.1007/s00382-022-06428-5, URL https://doi.org/10.1007/s00382-022-06428-5

European Union-Copernicus Marine Service (2022) Global ocean colour (copernicus-globcolour), bio-geo-chemical, l4 (monthly and interpolated) from satellite observations (1997-ongoing). https://doi.org/10.48670/MOI-00281, URL https://resources.marine.copernicus.eu/product-detail/OCEANCOLOUR_GLO_BGC_L4_MY_009_104/INFORMATION

Eyring V, Bony S, Meehl GA, et al (2016) Overview of the coupled model intercomparison project phase 6 (CMIP6) experimental design and organization. Geoscientific Model Development 9(5):1937–1958. https://doi.org/10.5194/gmd-9-1937-2016, URL https://doi.org/10.5194/gmd-9-1937-2016

Fay AR, McKinley GA (2014) Global open-ocean biomes: mean and temporal variability. Earth System Science Data 6(2):273–284. https://doi.org/10.5194/essd-6-273-2014, URL https://doi.org/10.5194/essd-6-273-2014

Fay AR, Gregor L, Landschützer P, et al (2021) Seaflux: harmonization of air–sea co_2 fluxes from surface pco_2 data products using a standardized approach. Earth System

Science Data 13(10):4693–4710. https://doi.org/10.5194/essd-13-4693-2021, URL https://doi.org/10.5194/essd-13-4693-2021

Feely RA, Takahashi T, Wanninkhof R, et al (2006) Decadal variability of the air-sea co2 fluxes in the equatorial pacific ocean. Journal of Geophysical Research: Oceans 111(C8). https://doi.org/10.1029/2005jc003129, URL http://dx.doi.org/10.1029/2005JC003129

Fetterer F, K. K, W. M, et al (2017) Sea ice index, version 3. https://doi.org/10.7265/N5K072F8, URL https://nsidc.org/data/G02135/versions/3

Fox-Kemper B, Ferrari R, Hallberg R (2008) Parameterization of mixed layer eddies. part i: Theory and diagnosis. Journal of Physical Oceanography 38(6):1145–1165. https://doi.org/10.1175/2007jpo3792.1, URL https://doi.org/10.1175/2007jpo3792.1

Fox-Kemper B, Danabasoglu G, Ferrari R, et al (2011) Parameterization of mixed layer eddies. iii: Implementation and impact in global ocean climate simulations. Ocean Modelling 39(1–2):61–78. https://doi.org/10.1016/j.ocemod.2010.09.002, URL http://dx.doi.org/10.1016/j.ocemod.2010.09.002

Friedlingstein P, O'Sullivan M, Jones MW, et al (2022) Global carbon budget 2022. Earth System Science Data 14(11):4811–4900. https://doi.org/10.5194/essd-14-4811-2022, URL https://doi.org/10.5194/essd-14-4811-2022

Fu W, Randerson JT, Moore JK (2016) Climate change impacts on net primary production (NPP) and export production (EP) regulated by increasing stratification and phytoplankton community structure in the CMIP5 models. Biogeosciences 13(18):5151–5170. https://doi.org/10.5194/bg-13-5151-2016, URL https://doi.org/10.5194/bg-13-5151-2016

Fu W, Moore JK, Primeau F, et al (2022) Evaluation of ocean biogeochemistry and carbon cycling in CMIP earth system models with the international ocean model benchmarking (IOMB) software system. Journal of Geophysical Research: Oceans 127(10). https://doi.org/10.1029/2022jc018965, URL https://doi.org/10.1029/2022jc018965

Gallego MA, Timmermann A, Friedrich T, et al (2018) Drivers of future seasonal cycle changes in oceanic pco2. Biogeosciences 15(17):5315–5327. https://doi.org/10.5194/bg-15-5315-2018, URL https://doi.org/10.5194/bg-15-5315-2018

Garbe CS, Rutgersson A, Boutin J, et al (2014) Transfer across the air-sea interface. Ocean-atmosphere interactions of gases and particles pp 55–112

Gaspar P, Grégoris Y, Lefevre JM (1990) A simple eddy kinetic energy model for simulations of the oceanic vertical mixing: Tests at station papa and long-term upper ocean study site. Journal of Geophysical Research: Oceans 95(C9):16179–16193. https://doi.org/https://doi.org/10.1029/JC095iC09p16179, URL https://agupubs.onlinelibrary.wiley.com/doi/abs/10.1029/JC095iC09p16179, https://agupubs.onlinelibrary.wiley.com/doi/pdf/10.1029/JC095iC09p16179

Gent PR, Mcwilliams JC (1990) Isopycnal mixing in ocean circulation models. Journal of Physical Oceanography 20(1):150 – 155. https://doi.org/https://doi.org/10.1175/1520-0485(1990)020<0150:IMIOCM>2.0.CO;2, URL https://journals.ametsoc.org/view/journals/phoc/20/1/1520-0485_1990_020_0150_imiocm_2_0_co_2.xml

Gent PR, Willebrand J, McDougall TJ, et al (1995) Parameterizing eddy-induced tracer transports in ocean circulation models. Journal of Physical Oceanography 25(4):463 – 474. https://doi.org/https://doi.org/10.1175/1520-0485(1995)025<0463:PEITTI>2.0.CO;2, URL https://journals.ametsoc.org/view/journals/

phoc/25/4/1520-0485_1995_025_0463_peitti_2_0_co_2.xml

Giorgetta M, Roeckner E, Mauritsen T, et al (2013) The atmospheric general circulation model ECHAM6 – model description. Reports on Earth System Science (135)

Gloege L, McKinley GA, Landschützer P, et al (2021) Quantifying errors in observationally based estimates of ocean carbon sink variability. Global Biogeochemical Cycles 35(4). https://doi.org/10.1029/2020gb006788, URL https://doi.org/10.1029/2020gb006788

Golaz J, Caldwell PM, Van Roekel LP, et al (2019) The doe e3sm coupled model version 1: Overview and evaluation at standard resolution. Journal of Advances in Modeling Earth Systems 11(7):2089–2129. https://doi.org/10.1029/2018ms001603, URL http://dx.doi.org/10.1029/2018MS001603

Good SA, Martin MJ, Rayner NA (2013) EN4: Quality controlled ocean temperature and salinity profiles and monthly objective analyses with uncertainty estimates. Journal of Geophysical Research: Oceans 118(12):6704–6716. https://doi.org/10.1002/2013jc009067, URL https://doi.org/10.1002/2013jc009067

Gooya P, Swart NC, Hamme RC (2023) Time-varying changes and uncertainties in the cmip6 ocean carbon sink from global to local scale. Earth System Dynamics 14(2):383–398. https://doi.org/10.5194/esd-14-383-2023, URL http://dx.doi.org/10.5194/esd-14-383-2023

Gouretski V, Cheng L (2020) Correction for systematic errors in the global dataset of temperature profiles from mechanical bathythermographs. Journal of Atmospheric and Oceanic Technology 37(5):841–855. https://doi.org/10.1175/jtech-d-19-0205.1, URL https://doi.org/10.1175/jtech-d-19-0205.1

Gouretski V, Reseghetti F (2010) On depth and temperature biases in bathythermograph data: Development of a new correction scheme based on analysis of a global ocean database. Deep Sea Research Part I: Oceanographic Research Papers 57(6):812–833. https://doi.org/10.1016/j.dsr.2010.03.011, URL https://doi.org/10.1016/j.dsr.2010.03.011

Gregor L, Fay A (2021) Seaflux: harmonised sea-air co2 fluxes from surface pco2 data products using a standardised approach. https://doi.org/10.5281/ZENODO.5482547, URL https://zenodo.org/record/5482547

Gregor L, Lebehot AD, Kok S, et al (2019) A comparative assessment of the uncertainties of global surface ocean CO_2 estimates using a machine-learning ensemble (csir-ml6 version 2019a) – have we hit the wall? Geoscientific Model Development 12(12):5113–5136. https://doi.org/10.5194/gmd-12-5113-2019, URL https://doi.org/10.5194/gmd-12-5113-2019

Griffies SM (2014) Elements of the Modular Ocean Model (MOM) (2012 release with updates). GFDL Ocean Group Technical Report No. 7

Griffies SM, Gnanadesikan A, Pacanowski RC, et al (1998) Isoneutral Diffusion in a z-Coordinate Ocean Model. Journal of Physical Oceanography 28(5):805–830. https://doi.org/10.1175/1520-0485(1998)028<0805:IDIAZC>2.0.CO;2

Griffies SM, Gnanadesikan A, Dixon KW, et al (2005) Formulation of an ocean model for global climate simulations. Ocean Science 1(1):45–79. https://doi.org/10.5194/os-1-45-2005, URL http://dx.doi.org/10.5194/os-1-45-2005

Gruber N, Clement D, Carter BR, et al (2019) The oceanic sink for anthropogenic CO_2 from 1994 to 2007. Science 363(6432):1193–1199. https://doi.org/10.1126/science.aau5153, URL http://dx.doi.org/10.1126/science.aau5153

Gruber N, Bakker DCE, DeVries T, et al (2023) Trends and variability in the ocean carbon sink. Nature Reviews Earth & Environment 4(2):119–134. https://doi.org/10.1038/s43017-022-00381-x, URL https://doi.org/10.1038/s43017-022-00381-x

Guo Y, Yu Y, Lin P, et al (2020) Overview of the cmip6 historical experiment datasets with the climate system model cas fgoals-f3-l. Advances in Atmospheric Sciences 37(10):1057–1066. https://doi.org/10.1007/s00376-020-2004-4, URL http://dx.doi.org/10.1007/s00376-020-2004-4

Gürses O, Oziel L, Karakuş O, et al (2023) Ocean biogeochemistry in the coupled ocean–sea ice–biogeochemistry model FESOM2.1–REcoM3. Geoscientific Model Development 16(16):4883–4936. https://doi.org/10.5194/gmd-16-4883-2023, URL https://doi.org/10.5194/gmd-16-4883-2023

Hagemann S, Dümenil L (1998) A parametrization of the lateral waterflow for the global scale. Climate Dynamics 14(1):17–31. https://doi.org/10.1007/s003820050205, URL https://doi.org/10.1007/s003820050205

Hajima T, Watanabe M, Yamamoto A, et al (2020) Development of the MIROC-ES2l earth system model and the evaluation of biogeochemical processes and feedbacks. Geoscientific Model Development 13(5):2197–2244. https://doi.org/10.5194/gmd-13-2197-2020, URL https://doi.org/10.5194/gmd-13-2197-2020

Hasumi H (2015) CCSR Ocean Component Model (COCO). URL https://ccsr.aori.u-tokyo.ac.jp/~hasumi/COCO/coco4.pdf, Version 4.0

Hauck J, Völker C, Wang T, et al (2013) Seasonally different carbon flux changes in the southern ocean in response to the southern annular mode. Global Biogeochemical Cycles 27(4):1236–1245. https://doi.org/https://doi.org/10.1002/2013GB004600, URL https://agupubs.onlinelibrary.wiley.com/doi/abs/10.1002/2013GB004600, https://agupubs.onlinelibrary.wiley.com/doi/pdf/10.1002/2013GB004600

Hauck J, Zeising M, Quéré CL, et al (2020) Consistency and challenges in the ocean carbon sink estimate for the global carbon budget. Frontiers in Marine Science 7. https://doi.org/10.3389/fmars.2020.571720, URL https://doi.org/10.3389/fmars.2020.571720

Hauck J, Nissen C, Landschützer P, et al (2023) Sparse observations induce large biases in estimates of the global ocean CO_2 sink: an ocean model subsampling experiment. Philosophical Transactions of the Royal Society A: Mathematical, Physical and Engineering Sciences 381(2249). https://doi.org/10.1098/rsta.2022.0063, URL https://doi.org/10.1098/rsta.2022.0063

Holte J, Talley L (2009) A new algorithm for finding mixed layer depths with applications to argo data and subantarctic mode water formation. Journal of Atmospheric and Oceanic Technology 26(9):1920–1939. https://doi.org/10.1175/2009jtecho543.1, URL https://doi.org/10.1175/2009jtecho543.1

Huang B, Liu C, Banzon V, et al (2021) Improvements of the daily optimum interpolation sea surface temperature (DOISST) version 2.1. Journal of Climate 34(8):2923–2939. https://doi.org/10.1175/jcli-d-20-0166.1, URL https://doi.org/10.1175/jcli-d-20-0166.1

Hurrell JW, Holland MM, Gent PR, et al (2013) The community earth system model: a framework for collaborative research. Bulletin of the American Meteorological Society 94(9):1339–1360

IOC, SCOR, IAPSO (2010) The international thermodynamic equation of seawater – 2010: Calculation and use of thermodynamic properties. No. 56 in Intergovernmental Oceanographic Commission, Manuals and Guides, UNESCO

Jiang LQ, Carter BR, Feely RA, et al (2019) Surface ocean pH and buffer capacity: past, present and future. Scientific Reports 9(1). https://doi.org/10.1038/s41598-019-55039-4, URL https://doi.org/10.1038/s41598-019-55039-4

Jones CD, Arora V, Friedlingstein P, et al (2016) C4mip – the coupled climate–carbon cycle model intercomparison project: experimental protocol for cmip6. Geoscientific Model Development 9(8):2853–2880. https://doi.org/10.5194/gmd-9-2853-2016, URL http://dx.doi.org/10.5194/gmd-9-2853-2016

Jungclaus JH, Fischer N, Haak H, et al (2013) Characteristics of the ocean simulations in the max planck institute ocean model (mpiom) the ocean component of the mpi-earth system model. Journal of Advances in Modeling Earth Systems 5(2):422–446. https://doi.org/https://doi.org/10.1002/jame.20023, URL https://agupubs.onlinelibrary.wiley.com/doi/abs/10.1002/jame.20023, https://agupubs.onlinelibrary.wiley.com/doi/pdf/10.1002/jame.20023

Jungclaus JH, Lorenz SJ, Schmidt H, et al (2022) The ICON earth system model version 1.0. J Adv Model Earth Syst 14(4)

Karakuş O, Völker C, Iversen M, et al (2021) Modeling the impact of macrozooplankton on carbon export production in the southern ocean. Journal of Geophysical Research: Oceans 126(12). https://doi.org/10.1029/2021jc017315, URL https://doi.org/10.1029/2021jc017315

Kelley D, Richards C, SCOR/IAPSO W (2022) gsw: Gibbs Sea Water Functions. URL https://CRAN.R-project.org/package=gsw, r package version 1.1-1

Kelley M, Schmidt GA, Nazarenko LS, et al (2020) GISS-E2.1: Configurations and climatology. J Adv Model Earth Syst 12(8):e2019MS002025

Keppler L, Landschützer P (2019) Regional wind variability modulates the southern ocean carbon sink. Scientific Reports 9(1). https://doi.org/10.1038/s41598-019-43826-y, URL https://doi.org/10.1038/s41598-019-43826-y

Kobayashi S, Ota Y, Harada Y, et al (2015) The JRA-55 reanalysis: General specifications and basic characteristics. Journal of the Meteorological Society of Japan Ser II 93(1):5–48. https://doi.org/10.2151/jmsj.2015-001, URL https://doi.org/10.2151/jmsj.2015-001

Koseki S, Tjiputra J, Fransner F, et al (2023) Disentangling the impact of atlantic niño on sea-air CO2 flux. Nature Communications 14(1). https://doi.org/10.1038/s41467-023-38718-9, URL https://doi.org/10.1038/s41467-023-38718-9

Kuhlbrodt T, Jones CG, Sellar A, et al (2018) The low-resolution version of hadgem3 gc3.1: Development and evaluation for global climate. Journal of Advances in Modeling Earth Systems 10(11):2865–2888. https://doi.org/https://doi.org/10.1029/2018MS001370, URL https://agupubs.onlinelibrary.wiley.com/doi/abs/10.1029/2018MS001370, https://agupubs.onlinelibrary.wiley.com/doi/pdf/10.1029/2018MS001370

Kwak K, Song H, Marshall J, et al (2021) Suppressed CO_2 in the southern ocean due to the interaction between current and wind. Journal of Geophysical Research: Oceans 126(12). https://doi.org/10.1029/2021jc017884, URL https://doi.org/10.1029/2021jc017884

Lacroix F, Ilyina T, Hartmann J (2020) Oceanic CO_2 outgassing and biological production hotspots induced by pre-industrial river loads of nutrients and carbon in a global modeling approach. Biogeosciences 17(1):55–88. https://doi.org/10.5194/bg-17-55-2020, URL https://doi.org/10.5194/bg-17-55-2020

Lan X, Tans P, Thoning K, et al (2023) Trends in globally-averaged co2 determined from noaa global monitoring laboratory measurements. https://doi.org/10.15138/9N0H-ZH07, URL https://gml.noaa.gov/ccgg/trends/global.html?doi=10.15138/9n0h-zh07

Landschützer P, Gruber N, Bakker DCE, et al (2018) Strengthening seasonal marine CO2 variations due to increasing atmospheric CO2. Nature Climate Change 8(2):146–150. https://doi.org/10.1038/s41558-017-0057-x, URL https://doi.org/10.1038/s41558-017-0057-x

Landschützer P, Ilyina T, Lovenduski NS (2019) Detecting regional modes of variability in observation-based surface ocean pco2. Geophysical Research Letters 46(5):2670–2679. https://doi.org/https://doi.org/10.1029/2018GL081756, URL https://agupubs.onlinelibrary.wiley.com/doi/abs/10.1029/2018GL081756, https://agupubs.onlinelibrary.wiley.com/doi/pdf/10.1029/2018GL081756

Large WG, McWilliams JC, Doney SC (1994) Oceanic vertical mixing: A review and a model with a nonlocal boundary layer parameterization. Reviews of Geophysics 32(4):363–403. https://doi.org/https://doi.org/10.1029/94RG01872, URL https://agupubs.onlinelibrary.wiley.com/doi/abs/10.1029/94RG01872, https://agupubs.onlinelibrary.wiley.com/doi/pdf/10.1029/94RG01872

Le Grix N, Zscheischler J, Laufkötter C, et al (2021) Compound high-temperature and low-chlorophyll extremes in the ocean over the satellite period. Biogeosciences 18(6):2119–2137. https://doi.org/10.5194/bg-18-2119-2021, URL https://bg.copernicus.org/articles/18/2119/2021/

Lee WL, Wang YC, Shiu CJ, et al (2020) Taiwan earth system model version 1: description and evaluation of mean state. Geoscientific Model Development 13(9):3887–3904

Li G, Cheng L, Zhu J, et al (2020) Increasing ocean stratification over the past half-century. Nature Climate Change 10(12):1116–1123. https://doi.org/10.1038/s41558-020-00918-2, URL https://doi.org/10.1038/s41558-020-00918-2

Li G, Cheng L, Wang X (2023) Evaluation of the cas-esm2-0 performance in simulating the global ocean salinity change. Atmosphere 14(1):107. https://doi.org/10.3390/atmos14010107, URL http://dx.doi.org/10.3390/atmos14010107

Li H, Ilyina T, Müller WA, et al (2019) Predicting the variable ocean carbon sink. Science Advances 5(4). https://doi.org/10.1126/sciadv.aav6471, URL https://doi.org/10.1126/sciadv.aav6471

Liao E, Resplandy L, Liu J, et al (2020) Amplification of the ocean carbon sink during el niños: Role of poleward ekman transport and influence on atmospheric co2. Global Biogeochemical Cycles 34(9). https://doi.org/10.1029/2020gb006574, URL http://dx.doi.org/10.1029/2020GB006574

Lin Y, Huang X, Liang Y, et al (2020) Community integrated earth system model (ciesm): Description and evaluation. Journal of Advances in Modeling Earth Systems 12(8). https://doi.org/10.1029/2019ms002036, URL http://dx.doi.org/10.1029/2019MS002036

Liu H, Lin P, Yu Y, et al (2012) The baseline evaluation of lasg/iap climate system ocean model (licom) version 2. Acta Meteorologica Sinica 26(3):318–329. https://doi.org/10.1007/s13351-012-0305-y, URL http://dx.doi.org/10.1007/s13351-012-0305-y

Liu Y, Moore JK, Primeau F, et al (2022) Reduced CO2 uptake and growing nutrient sequestration from slowing overturning circulation. Nature Climate Change 13(1):83–90. https://doi.org/10.1038/s41558-022-01555-7, URL https://doi.org/10.

1038/s41558-022-01555-7

Löptien U, Dietze H (2019) Reciprocal bias compensation and ensuing uncertainties in model-based climate projections: pelagic biogeochemistry versus ocean mixing. Biogeosciences 16(9):1865–1881. https://doi.org/10.5194/bg-16-1865-2019, URL https://doi.org/10.5194/bg-16-1865-2019

Lovato T, Peano D, Butenschön M, et al (2022) Cmip6 simulations with the cmcc earth system model (cmcc-esm2). Journal of Advances in Modeling Earth Systems 14(3). https://doi.org/10.1029/2021ms002814, URL http://dx.doi.org/10.1029/2021MS002814

Lovenduski NS, Gruber N, Doney SC, et al (2007) Enhanced CO_2 outgassing in the southern ocean from a positive phase of the southern annular mode. Global Biogeochemical Cycles 21(2). https://doi.org/10.1029/2006gb002900, URL https://doi.org/10.1029/2006gb002900

Lovenduski NS, Yeager SG, Lindsay K, et al (2019) Predicting near-term variability in ocean carbon uptake. Earth System Dynamics 10(1):45–57. https://doi.org/10.5194/esd-10-45-2019, URL https://doi.org/10.5194/esd-10-45-2019

Marsland S, Haak H, Jungclaus J, et al (2003) The max-planck-institute global ocean/sea ice model with orthogonal curvilinear coordinates. Ocean Modelling 5(2):91–127. https://doi.org/https://doi.org/10.1016/S1463-5003(02)00015-X, URL https://www.sciencedirect.com/science/article/pii/S146350030200015X

Mauritsen T, Bader J, Becker T, et al (2019) Developments in the mpi-m earth system model version 1.2 (mpi-esm1.2) and its response to increasing co2. Journal of Advances in Modeling Earth Systems 11(4):998–1038. https://doi.org/https://doi.org/10.1029/2018MS001400, URL https://agupubs.onlinelibrary.wiley.com/doi/abs/10.1029/2018MS001400, https://agupubs.onlinelibrary.wiley.com/doi/pdf/10.1029/2018MS001400

Mayot N, Quéré CL, Rödenbeck C, et al (2023) Climate-driven variability of the southern ocean co_2 sink. Philosophical Transactions of the Royal Society A: Mathematical, Physical and Engineering Sciences 381(2249). https://doi.org/10.1098/rsta.2022.0055, URL https://doi.org/10.1098/rsta.2022.0055

McDougall TJ, Dewar WK (1998) Vertical mixing and cabbeling in layered models. Journal of Physical Oceanography 28(7):1458–1480. https://doi.org/10.1175/1520-0485(1998)028<1458:vmacil>2.0.co;2, URL http://dx.doi.org/10.1175/1520-0485(1998)028<1458:VMACIL>2.0.CO;2

McKinley GA, Follows MJ, Marshall J (2004) Mechanisms of air-sea CO_2 flux variability in the equatorial pacific and the north atlantic. Global Biogeochemical Cycles 18(2). https://doi.org/10.1029/2003gb002179, URL https://doi.org/10.1029/2003gb002179

McKinley GA, Fay AR, Lovenduski NS, et al (2017) Natural variability and anthropogenic trends in the ocean carbon sink. Annual Review of Marine Science 9(1):125–150. https://doi.org/10.1146/annurev-marine-010816-060529, URL https://doi.org/10.1146/annurev-marine-010816-060529

McKinley GA, Fay AR, Eddebbar YA, et al (2020) External forcing explains recent decadal variability of the ocean carbon sink. AGU Advances 1(2). https://doi.org/10.1029/2019av000149, URL https://doi.org/10.1029/2019av000149

Meinshausen M, Vogel E, Nauels A, et al (2017) Historical greenhouse gas concentrations for climate modelling (CMIP6). Geoscientific Model Development 10(5):2057–2116. https://doi.org/10.5194/gmd-10-2057-2017, URL https://doi.org/10.5194/

gmd-10-2057-2017

Mellor GL, Yamada T (1982) Development of a turbulence closure model for geophysical fluid problems. Reviews of Geophysics 20(4):851–875. https://doi.org/10.1029/rg020i004p00851, URL http://dx.doi.org/10.1029/RG020i004p00851

Melnikova I, Boucher O, Cadule P, et al (2021) Carbon cycle response to temperature overshoot beyond 2°c: An analysis of CMIP6 models. Earth's Future 9(5). https://doi.org/10.1029/2020ef001967, URL https://doi.org/10.1029/2020ef001967

Meyssignac B, Boyer T, Zhao Z, et al (2019) Measuring global ocean heat content to estimate the earth energy imbalance. Frontiers in Marine Science 6. https://doi.org/10.3389/fmars.2019.00432, URL https://doi.org/10.3389/fmars.2019.00432

Morrison AK, Waugh DW, Hogg AM, et al (2022) Ventilation of the southern ocean pycnocline. Annual Review of Marine Science 14(1):405–430. https://doi.org/10.1146/annurev-marine-010419-011012, URL https://doi.org/10.1146/annurev-marine-010419-011012

Nicholson SA, Whitt DB, Fer I, et al (2022) Storms drive outgassing of CO2 in the subpolar southern ocean. Nature Communications 13(1). https://doi.org/10.1038/s41467-021-27780-w, URL https://doi.org/10.1038/s41467-021-27780-w

Noh Y, Jin Kim H (1999) Simulations of temperature and turbulence structure of the oceanic boundary layer with the improved near-surface process. Journal of Geophysical Research: Oceans 104(C7):15621–15634. https://doi.org/https://doi.org/10.1029/1999JC900068, URL https://agupubs.onlinelibrary.wiley.com/doi/abs/10.1029/1999JC900068, https://agupubs.onlinelibrary.wiley.com/doi/pdf/10.1029/1999JC900068

Oberhuber JM (1993) Simulation of the atlantic circulation with a coupled sea ice-mixed layer-isopycnal general circulation model. part i: Model description. Journal of Physical Oceanography 23(5):808–829

O'Neill BC, Tebaldi C, van Vuuren DP, et al (2016) The scenario model intercomparison project (ScenarioMIP) for CMIP6. Geoscientific Model Development 9(9):3461–3482. https://doi.org/10.5194/gmd-9-3461-2016, URL https://doi.org/10.5194/gmd-9-3461-2016

Orr JC, Najjar RG, Aumont O, et al (2017) Biogeochemical protocols and diagnostics for the CMIP6 ocean model intercomparison project (OMIP). Geoscientific Model Development 10(6):2169–2199. https://doi.org/10.5194/gmd-10-2169-2017, URL https://doi.org/10.5194/gmd-10-2169-2017

Pacanowski RC, Philander SGH (1981) Parameterization of vertical mixing in numerical models of tropical oceans. Journal of Physical Oceanography 11(11):1443–1451. https://doi.org/10.1175/1520-0485(1981)011<1443:povmin>2.0.co;2, URL https://doi.org/10.1175/1520-0485(1981)011<1443:povmin>2.0.co;2

Pan R, Shu Q, Wang Q, et al (2023) Future arctic climate change in CMIP6 strikingly intensified by NEMO-family climate models. Geophysical Research Letters 50(4). https://doi.org/10.1029/2022gl102077, URL https://doi.org/10.1029/2022gl102077

Park S, Shin J, Kim S, et al (2019) Global climate simulated by the seoul national university atmosphere model version 0 with a unified convection scheme (sam0-unicon). Journal of Climate 32(10):2917–2949

Petersen MR, Asay-Davis XS, Berres AS, et al (2019) An evaluation of the ocean and sea ice climate of e3sm using mpas and interannual core-ii forcing. Journal of Advances in Modeling Earth Systems 11(5):1438–1458. https://doi.org/10.1029/

2018ms001373, URL http://dx.doi.org/10.1029/2018MS001373

Prend CJ, Gray AR, Talley LD, et al (2022) Indo-pacific sector dominates southern ocean carbon outgassing. Global Biogeochemical Cycles 36(7). https://doi.org/10.1029/2021gb007226, URL https://doi.org/10.1029/2021gb007226

Rahmstorf S (1993) A fast and complete convection scheme for ocean models. Ocean Modelling 101:9–11

Rayner NA (2003) Global analyses of sea surface temperature, sea ice, and night marine air temperature since the late nineteenth century. Journal of Geophysical Research 108(D14). https://doi.org/10.1029/2002jd002670, URL https://doi.org/10.1029/2002jd002670

Redi MH (1982) Oceanic Isopycnal Mixing by Coordinate Rotation. Journal of Physical Oceanography 12(10):1154–1158. https://doi.org/10.1175/1520-0485(1982)012<1154:OIMBCR>2.0.CO;2

Reichl BG, Hallberg R (2018) A simplified energetics based planetary boundary layer (ePBL) approach for ocean climate simulations. Ocean Modelling 132:112–129. https://doi.org/10.1016/j.ocemod.2018.10.004, URL https://doi.org/10.1016/j.ocemod.2018.10.004

Reick CH, Gayler V, Goll D, et al (2021) Jsbach 3 – the land component of the mpi earth system model. documentation of version 3.2. Reports on Earth System Science (240). https://doi.org/10.17617/2.3279802

Roberts MJ, Baker A, Blockley EW, et al (2019) Description of the resolution hierarchy of the global coupled HadGEM3-GC3.1 model as used in CMIP6 HighResMIP experiments. Geosci Model Dev 12(12):4999–5028

Rödenbeck C, DeVries T, Hauck J, et al (2022) Data-based estimates of interannual sea–air co_2 flux variations 1957–2020 and their relation to environmental drivers. Biogeosciences 19(10):2627–2652. https://doi.org/10.5194/bg-19-2627-2022, URL https://doi.org/10.5194/bg-19-2627-2022

Romanou A, Gregg WW, Romanski J, et al (2013) Natural air–sea flux of CO2 in simulations of the NASA-GISS climate model: Sensitivity to the physical ocean model formulation. Ocean Model (Oxf) 66:26–44

Rong X (2019) Cams cams-csm1.0 model output prepared for cmip6 scenariomip. https://doi.org/10.22033/ESGF/CMIP6.11004, URL https://doi.org/10.22033/ESGF/CMIP6.11004

Sabine CL, Feely RA, Gruber N, et al (2004) The oceanic sink for anthropogenic CO_2. Science 305(5682):367–371. https://doi.org/10.1126/science.1097403, URL https://doi.org/10.1126/science.1097403

Saenko OA, Yang D, Gregory JM (2018) Impact of mesoscale eddy transfer on heat uptake in an eddy-parameterizing ocean model. Journal of Climate 31(20):8589–8606. https://doi.org/10.1175/jcli-d-18-0186.1, URL https://doi.org/10.1175/jcli-d-18-0186.1

Sallée JB, Shuckburgh E, Bruneau N, et al (2013) Assessment of southern ocean mixed-layer depths in CMIP5 models: Historical bias and forcing response. Journal of Geophysical Research: Oceans 118(4):1845–1862. https://doi.org/10.1002/jgrc.20157, URL https://doi.org/10.1002/jgrc.20157

Sallée JB, Pellichero V, Akhoudas C, et al (2021) Summertime increases in upper-ocean stratification and mixed-layer depth. Nature 591(7851):592–598. https://doi.org/10.1038/s41586-021-03303-x, URL https://doi.org/10.1038/

s41586-021-03303-x

Sathyendranath S, Brewin R, Brockmann C, et al (2019) An ocean-colour time series for use in climate studies: The experience of the ocean-colour climate change initiative (OC-CCI). Sensors 19(19):4285. https://doi.org/10.3390/s19194285, URL https://doi.org/10.3390/s19194285

Schmidt GA, Kelley M, Nazarenko L, et al (2014) Configuration and assessment of the GISS ModelE2 contributions to the CMIP5 archive. J Adv Model Earth Syst 6(1):141–184

Schneider B, Bopp L, Gehlen M, et al (2008) Climate-induced interannual variability of marine primary and export production in three global coupled climate carbon cycle models. Biogeosciences 5(2):597–614. https://doi.org/10.5194/bg-5-597-2008, URL https://doi.org/10.5194/bg-5-597-2008

Schourup-Kristensen V, Sidorenko D, Wolf-Gladrow DA, et al (2014) A skill assessment of the biogeochemical model REcoM2 coupled to the finite element sea ice–ocean model (FESOM 1.3). Geoscientific Model Development 7(6):2769–2802. https://doi.org/10.5194/gmd-7-2769-2014, URL https://doi.org/10.5194/gmd-7-2769-2014

Schulz M, Mudelsee M (2002) Redfit: estimating red-noise spectra directly from unevenly spaced paleoclimatic time series. Computers & Geosciences 28(3):421–426. https://doi.org/https://doi.org/10.1016/S0098-3004(01)00044-9, URL https://www.sciencedirect.com/science/article/pii/S0098300401000449

Schulzweida U (2022) Cdo user guide. https://doi.org/10.5281/zenodo.7112925, URL https://doi.org/10.5281/zenodo.7112925

Séférian R, Nabat P, Michou M, et al (2019) Evaluation of CNRM earth system model, CNRM-ESM2-1: Role of earth system processes in present-day and future climate. Journal of Advances in Modeling Earth Systems 11(12):4182–4227. https://doi.org/10.1029/2019ms001791, URL https://doi.org/10.1029/2019ms001791

Seland Ø, Bentsen M, Olivié D, et al (2020) Overview of the norwegian earth system model (noresm2) and key climate response of cmip6 deck, historical, and scenario simulations. Geoscientific Model Development 13(12):6165–6200

Sellar AA, Jones CG, Mulcahy JP, et al (2019) Ukesm1: Description and evaluation of the u.k. earth system model. Journal of Advances in Modeling Earth Systems 11(12):4513–4558. https://doi.org/https://doi.org/10.1029/2019MS001739, URL https://agupubs.onlinelibrary.wiley.com/doi/abs/10.1029/2019MS001739, https://agupubs.onlinelibrary.wiley.com/doi/pdf/10.1029/2019MS001739

Semmler T, Danilov S, Gierz P, et al (2020) Simulations for CMIP6 with the AWI climate model AWI-CM-1-1. Journal of Advances in Modeling Earth Systems 12(9). https://doi.org/10.1029/2019ms002009, URL https://doi.org/10.1029/2019ms002009

Sepulchre P, Caubel A, Ladant JB, et al (2020) IPSL-CM5A2 – an earth system model designed for multi-millennial climate simulations. Geosci Model Dev 13(7):3011–3053

Small RJ, DuVivier AK, Whitt DB, et al (2020) On the control of subantarctic stratification by the ocean circulation. Climate Dynamics 56(1-2):299–327. https://doi.org/10.1007/s00382-020-05473-2, URL https://doi.org/10.1007/s00382-020-05473-2

Steele M, Morley R, Ermold W (2001) Phc: A global ocean hydrography with a high-quality arctic ocean. Journal of Climate 14(9):2079–2087. https://doi.

org/10.1175/1520-0442(2001)014<2079:pagohw>2.0.co;2, URL http://dx.doi.org/10.1175/1520-0442(2001)014<2079:PAGOHW>2.0.CO;2

Stevens B, Giorgetta M, Esch M, et al (2013) Atmospheric component of the mpi-m earth system model: Echam6. Journal of Advances in Modeling Earth Systems 5(2):146–172. https://doi.org/https://doi.org/10.1002/jame.20015, URL https://agupubs.onlinelibrary.wiley.com/doi/abs/10.1002/jame.20015, https://agupubs.onlinelibrary.wiley.com/doi/pdf/10.1002/jame.20015

Storkey D, Blaker AT, Mathiot P, et al (2018) Uk global ocean go6 and go7: a traceable hierarchy of model resolutions. Geoscientific Model Development 11(8):3187–3213. https://doi.org/10.5194/gmd-11-3187-2018, URL https://gmd.copernicus.org/articles/11/3187/2018/

Sun S, Bleck R (2006) Multi-century simulations with the coupled GISS–HYCOM climate model: control experiments. Clim Dyn 26(4):407–428

Sutton AJ, Feely RA, Sabine CL, et al (2014) Natural variability and anthropogenic change in equatorial pacific surface ocean pco2 and ph. Global Biogeochemical Cycles 28(2):131–145. https://doi.org/10.1002/2013gb004679, URL http://dx.doi.org/10.1002/2013GB004679

Swart NC, Cole JNS, Kharin VV, et al (2019) The canadian earth system model version 5 (CanESM5.0.3). Geoscientific Model Development 12(11):4823–4873. https://doi.org/10.5194/gmd-12-4823-2019, URL https://doi.org/10.5194/gmd-12-4823-2019

Takahashi T, Olafsson J, Goddard JG, et al (1993) Seasonal variation of co_2 and nutrients in the high-latitude surface oceans: A comparative study. Global Biogeochemical Cycles 7(4):843–878. https://doi.org/10.1029/93gb02263, URL https:

//doi.org/10.1029/93gb02263

Takahashi T, Sutherland SC, Sweeney C, et al (2002) Global sea–air CO2 flux based on climatological surface ocean pCO2, and seasonal biological and temperature effects. Deep Sea Research Part II: Topical Studies in Oceanography 49(9-10):1601–1622. https://doi.org/10.1016/s0967-0645(02)00003-6, URL https://doi.org/10.1016/s0967-0645(02)00003-6

Talley L, Feely R, Sloyan B, et al (2016) Changes in ocean heat, carbon content, and ventilation: A review of the first decade of GO-SHIP global repeat hydrography. Annual Review of Marine Science 8(1):185–215. https://doi.org/10.1146/annurev-marine-052915-100829, URL https://doi.org/10.1146/annurev-marine-052915-100829

Tatebe H, Ogura T, Nitta T, et al (2019) Description and basic evaluation of simulated mean state, internal variability, and climate sensitivity in MIROC6. Geosci Model Dev 12(7):2727–2765

Taylor KE, Juckes M, Balaji V, et al (2018) CMIP6 Global Attributes, DRS, Filenames, Directory Structure, and CV's. URL https://goo.gl/v1drZl, v6.2.7

Terhaar J, Frölicher TL, Joos F (2022) Observation-constrained estimates of the global ocean carbon sink from earth system models. Biogeosciences 19(18):4431–4457. https://doi.org/10.5194/bg-19-4431-2022, URL https://doi.org/10.5194/bg-19-4431-2022

Timmermann A, An SI, Kug JS, et al (2018) El niño–southern oscillation complexity. Nature 559(7715):535–545. https://doi.org/10.1038/s41586-018-0252-6, URL https://doi.org/10.1038/s41586-018-0252-6

Timmermann R, Danilov S, Schröter J, et al (2009) Ocean circulation and sea ice distribution in a finite element global sea ice–ocean model. Ocean Modelling 27(3-4):114–129. https://doi.org/10.1016/j.ocemod.2008.10.009, URL https://doi.org/10.1016/j.ocemod.2008.10.009

Tsujino H, Nakano H, Sakamoto K, et al (2017) Reference manual for the meteorological research institute community ocean model version 4 (mri. comv4). Technical Reports of the Meteorological Research Institute 80:306

Umlauf L, Burchard H (2003) A generic length-scale equation for geophysical turbulence models. Journal of Marine Research 61(2):235–265. https://doi.org/10.1357/002224003322005087, URL http://dx.doi.org/10.1357/002224003322005087

Vaittinada Ayar P, Bopp L, Christian JR, et al (2022) Contrasting projections of the enso-driven co_2 flux variability in the equatorial pacific under high-warming scenario. Earth System Dynamics 13(3):1097–1118. https://doi.org/10.5194/esd-13-1097-2022, URL https://esd.copernicus.org/articles/13/1097/2022/

Valcke S, Craig T, Coquart L (2015) OASIS3-MCT User Guide. URL http://oasis.enes.org, CERFACS/CNRS SUC URA No1875

Voldoire A, Saint-Martin D, Sénési S, et al (2019) Evaluation of CMIP6 DECK experiments with CNRM-CM6-1. Journal of Advances in Modeling Earth Systems 11(7):2177–2213. https://doi.org/10.1029/2019ms001683, URL https://doi.org/10.1029/2019ms001683

Volodin EM, Mortikov EV, Kostrykin SV, et al (2017) Simulation of the present-day climate with the climate model INMCM5. Clim Dyn 49(11-12):3715–3734

Wang Q, Danilov S, Schröter J (2008) Finite element ocean circulation model based on triangular prismatic elements, with application in studying the effect of topography representation. Journal of Geophysical Research 113(C5). https://doi.org/10.1029/2007jc004482, URL https://doi.org/10.1029/2007jc004482

Wang Q, Danilov S, Sidorenko D, et al (2014) The finite element sea ice-ocean model (FESOM) v.1.4: formulation of an ocean general circulation model. Geoscientific Model Development 7(2):663–693. https://doi.org/10.5194/gmd-7-663-2014, URL https://doi.org/10.5194/gmd-7-663-2014

Wanninkhof R (1992) Relationship between wind speed and gas exchange over the ocean. Journal of Geophysical Research: Oceans 97(C5):7373–7382. https://doi.org/https://doi.org/10.1029/92JC00188, URL https://agupubs.onlinelibrary.wiley.com/doi/abs/10.1029/92JC00188, https://agupubs.onlinelibrary.wiley.com/doi/pdf/10.1029/92JC00188

Wanninkhof R (2014) Relationship between wind speed and gas exchange over the ocean revisited. Limnology and Oceanography: Methods 12(6):351–362. https://doi.org/https://doi.org/10.4319/lom.2014.12.351, URL https://aslopubs.onlinelibrary.wiley.com/doi/abs/10.4319/lom.2014.12.351, https://aslopubs.onlinelibrary.wiley.com/doi/pdf/10.4319/lom.2014.12.351

Wu T, Zhang F, Zhang J, et al (2020) Beijing climate center earth system model version 1 (bcc-esm1): model description and evaluation of aerosol simulations. Geoscientific Model Development 13(3):977–1005. https://doi.org/10.5194/gmd-13-977-2020, URL http://dx.doi.org/10.5194/gmd-13-977-2020

Wu Y, Hain MP, Humphreys MP, et al (2019) What drives the latitudinal gradient in open-ocean surface dissolved inorganic carbon concentration? Biogeosciences 16(13):2661–2681. https://doi.org/10.5194/bg-16-2661-2019, URL https://doi.org/10.5194/bg-16-2661-2019

Yukimoto S, Kawai H, Koshiro T, et al (2019) The meteorological research institute earth system model version 2.0, MRI-ESM2.0: Description and basic evaluation of the physical component. J Meteorol Soc Japan 97(5):931–965

Zalesny VB, Marchuk GI, Agoshkov VI, et al (2010) Numerical simulation of large-scale ocean circulation based on the multicomponent splitting method. Russian J Numer Anal Math Modelling 25(6)

Ziehn T, Chamberlain MA, Law RM, et al (2020) The australian earth system model: Access-esm1.5. Journal of Southern Hemisphere Earth Systems Science 70(1):193–214. https://doi.org/10.1071/es19035, URL http://dx.doi.org/10.1071/ES19035

Zuur AF, Ieno EN, Smith GM (2007) Analysing Ecological Data. Springer New York, https://doi.org/10.1007/978-0-387-45972-1, URL https://doi.org/10.1007/978-0-387-45972-1

Statements and Declarations

Funding. This work was supported by the Initiative and Networking Fund of the Helmholtz Association (Helmholtz Young Investigator Group Marine Carbon and Ecosystem Feedbacks in the Earth System [MarESys], Grant VH-NG-1301) and by the ERC-2022-STG OceanPeak (Grant 101077209).

Competing Interests. The authors have no relevant financial or non-financial interests to disclose.

Author Contributions. All authors contributed to the study conception and design. Material preparation, data collection and analysis were performed by Christopher Danek. The first draft of the manuscript was written by Christopher Danek and all authors commented on previous versions of the manuscript. All authors read and approved the final manuscript.

Data Availability. The datasets generated during and/or analysed during the current study are available from the corresponding author on request.